

Chapter 14

Raman Imaging of Biomedical Samples



**Agnieszka Kaczor, Katarzyna M. Marzec, Katarzyna Majzner,
Kamila Kochan, Marta Z. Pacia and Malgorzata Baranska**

Abstract Fluorescence microscopy, a gold standard in the tissue or cell imaging, has several drawbacks, with a severe one being its disability to elucidate the chemical characteristics of the sample. Confocal Raman microscopy is a tempting label free alternative to fluorescence and a prospective future method of medical diagnostics. Raman measurements of tissues can provide information about their chemical composition, i.e. main components but also specific compounds, and their changes upon the development of patholog or its treatment. The analysis is based on characteristic marker bands, provided they can be identified in the spectra, or by more common approach using chemometrics. Moreover, Raman microscopy can be used to detect small biochemical alterations and their respective distribution in a single cell or even at sub-cellular level. The impact of various factors, including the uptake of drugs, bioactive compounds or non-chemical stressors can be observed using such investigations of cells.

14.1 Introduction

In this chapter the reader can find several examples of tissues (PART I; Sect. 14.2) and cells (PART II; Sect. 14.3) imaging using Raman spectroscopy and microscopy combined with other complementary or reference methods. Each part begins with an *Experimental* section, where details on the sample preparation,

A. Kaczor · K. Majzner · K. Kochan · M. Z. Pacia · M. Baranska (✉)
Faculty of Chemistry, Jagiellonian University, Ingardena 3,
30-060 Krakow, Poland
e-mail: baranska@chemia.uj.edu.pl

A. Kaczor · K. M. Marzec · K. Majzner · K. Kochan · M. Z. Pacia
M. Baranska
Jagiellonian Centre for Experimental Therapeutics, Jagiellonian University,
Bobrzynskiego 14, 30-348 Krakow, Poland

K. M. Marzec
Center for Medical Genomics (OMICRON), Jagiellonian University
Medical College, Kopernika 7C, 31-034 Krakow, Poland

data acquisition and data analysis are provided. That is followed by a *Results and Discussion* section, where biochemical analysis of various tissues or cells is discussed in the context of diagnosis and treatment of some modern lifestyle diseases.

In PART I (Sect. 14.2), various approaches for imaging the tissues from murine models of diseases of affluence are shown. Hypertension, atherosclerosis or diabetes are related to alterations in the vessel wall and, particularly, in the endothelium, the innermost layer (*tunica intima*) of the vessel wall separating the *tunica media* (smooth muscle cells with elastin and collagenous components) from the lumen of the blood vessel. Since the endothelial dysfunction is an early feature of such pathologies, the implementation of Raman imaging to study diseases of affluence is, therefore, aimed at identifying subtle differences in chemical and structural composition and in distribution of components in the endothelium.

The key issue in studying thin tissue layers, such as endothelium, is the clear assignment of their signal. Conventional cross-section preparation yields information about the whole vessel wall. However, sometimes this is not practical, as extraction of the signal from the endothelial layer of the thickness of about 1 μm is complicated (practically the information has to be read out from 1–2 voxels). The additional problem is the fact, that a delicate endothelial layer, intrinsically uneven, can be even more perturbed due to microtome section cutting. Therefore, as an alternative, we adopted so-called *en face* preparation, previously used in scanning electron microscopy (SEM) [1–3] and atomic force microscopy (AFM) [4, 5] studies, in which the accessible surface of the endothelium is large and easy to image. In our developed methodology, *en face* tissue, in which the vessel wall is resected and split open, was submitted to combined Raman and AFM imaging [6]. Additionally, application of depth profiling combined with the independent analysis of subsequent layers enabled to define changes in the endothelium and *tunica media*, separately [7]. So, depending on the scientific aim, either cross-section or *en face* preparation was applied.

The verification of applicability of the combined Raman-AFM approach to study vessel walls and to recognize key cellular compartments was done based on the comparison with fluorescence imaging (Fig. 14.1) [8].

Figure 14.1 demonstrates that confocal Raman distribution images are in perfect agreement with the images of the immunochemically stained tissue, clearly visualizing distribution of key cellular components and compartments. Additionally, AFM data complement Raman images with information about the tissue topography and compressibility.

In PART II (Sect. 14.3), the potential of Raman imaging of single cells is discussed. With Raman microscopy we can detect small biochemical changes and their distribution at the sub-cellular level [9]. Investigations of cells allow tracking of changes under the impact of various factors, e.g. monitoring the uptake of drugs, nanoparticles and bioactive compounds, as well as non-chemical stressors [10–14]. Raman measurements with spatial resolution $\sim 300\text{nm}$ (limited by Rayleigh criterion) allow for detection and characterization of such small structures as nucleolus, nucleoli, mitochondria, lipid droplets (LDs; or lipid bodies) or introduced nanoparticles [15–18].

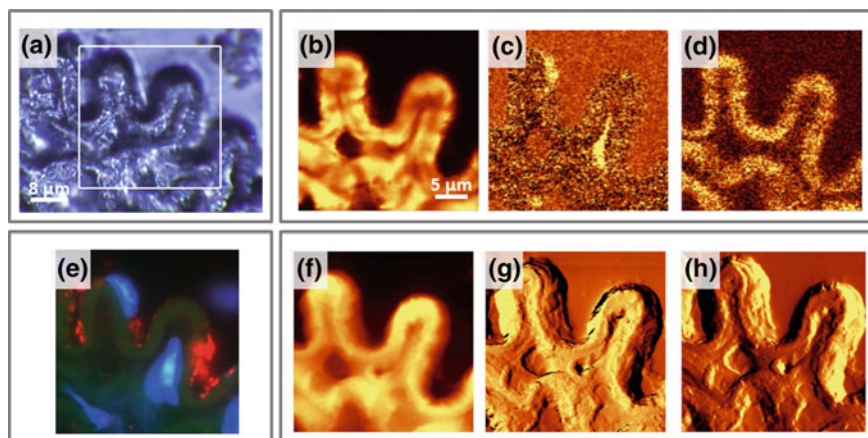


Fig. 14.1 Comparison of Raman-AFM combined imaging with fluorescence imaging of a vessel wall cross-section: The visual image [$\times 100$, (a)], Raman images showing distribution of organic matter (b), cell nuclei (c) and elastin fibres (d), fluorescence images of immunostained tissue (e), red, blue and green denote endothelium, nuclei and elastin fibres, respectively), topography image (f), phase image (g) and amplitude image (h)

In cell biology most commonly used methods are electron microscopy and fluorescence microscopy. Each of these techniques requires a specific sample preparation, thus modifying sample composition and changing its physiological conditions. With Raman microscopy, changes in the cells during the cell cycle, cell death, drug-cell interactions, proliferation and differentiation can be successfully studied avoiding the above mentioned modifications [19, 20].

14.2 Part I

14.2.1 Experimental

14.2.1.1 Sample Preparation

For diabetes, hypertension and cancer metastasis, the samples were resected from a thoracic fragment of the murine aorta.¹ Two types of sample preparation were used: cross-section of aorta and aorta *en face* (split open, Fig. 14.2).

For the cross-section preparation, the samples were fixed for 10 min in 4% buffered formalin (Merck), embedded in optimal cutting temperature (OCT) medium

¹All procedures involving animals were conducted in accordance with the Guidelines for Animal Care and Treatment of the European Union and were approved by the 1st Local Animal Ethics Commission in Krakow (decision no. 51/2009).

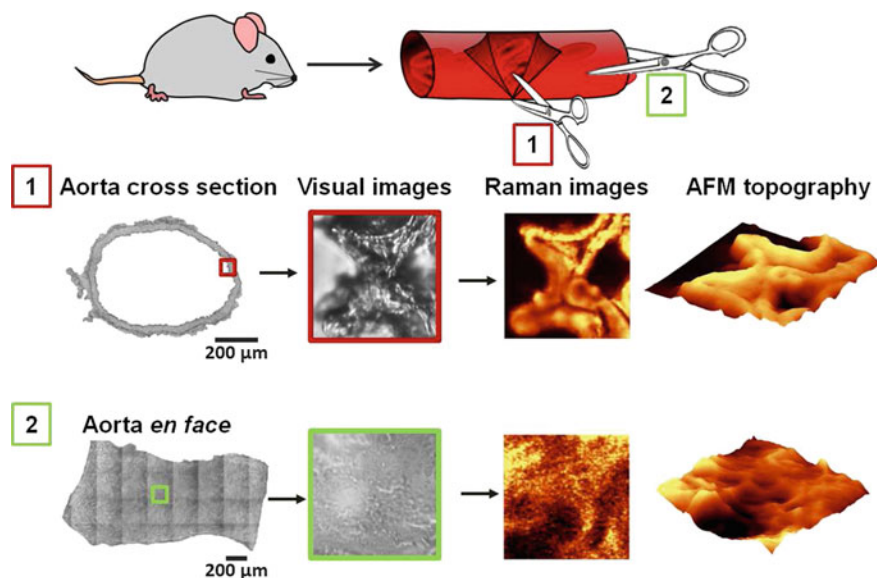


Fig. 14.2 Schematic illustration of methodology of sample preparation and measurement: Cross-sections of aorta (1) or resected and split-open aorta fragments (2) were mounted on CaF_2 slides. For cross-section samples, the area of the sample was chosen in a way to allow imaging of the inner-most (endothelium) part. Samples were submitted to Raman imaging and (in selected cases) subsequent AFM imaging

(Thermo) and frozen at -80°C . Cross-sections of $5\mu\text{m}$ thickness were cut with the microtome and mounted onto cell-Tak[®]-coated calcium fluoride slides. For *en face* preparation, the resected and split-open fragments of arteries were tightly glued to the cell-Tak[®]-coated calcium fluoride slides. Then tissues were preserved by a 10 min soak in 4% buffered formalin (Merck) and rinsed twice with distilled water.

For fluorescent detection of endothelial caveolin-1 (murine model of diabetes type 2) the tissue sections, prepared by blocking reagent and pre-incubation, were incubated with polyclonal rabbit anti-caveolin-1 antibody (Sigma) and cholera toxin B subunit (Sigma). Nuclei were stained using a Hoechst 33258 solution (Sigma).

For the examples of atherosclerosis plaque studies presented here, the cross-sections of brachiocephalic arteries (BCA) with visible lesions were taken from ApoE/LDLR^{-/-} mice of different ages or with different types of diets (chow, AIN-93G, LCHP). As the same cross-sections were used for co-localized IR, Raman, AFM and staining, a routine methodology was defined in the following way. The isolated BCA were fixed for 6 h in 4% buffered formalin. After fixation, BCA were mounted for further 6 h in a tissue freezing medium (Leica, Germany) with distilled water (1:1) and finally embedded in the OCT medium and frozen at -80°C . The 5 mm thick cross-section slides were put on CaF_2 slides. OCT was washed out before measurements.

For liver tissue sections the following procedure of sample preparation was used: immediately after collection, livers were embedded in OCT medium and frozen at -80°C . Immediately prior to the measurements, livers were cut into sections of $10\mu\text{m}$ thickness in a cryostat chamber (-23°C) and placed on CaF_2 slides. Tissues were preserved using 4% buffered formalin solution (10 min). The remainder of the fixative and OCT were washed out with distilled water (2×5 min).

Tissue sections were measured directly after preparation. If necessary, they were stored no longer than 48 h, ensuring conditions of zerolight exposure, as it is known that light and time strongly affect the unsaturation degree of lipids [21].

14.2.1.2 Data Acquisition

Raman imaging was done using the WITec alpha300 Raman microscope, which was equipped with an air cooled solid-state laser operating at 532 nm and a CCD detector (cooled to -65°C). The laser was coupled to the microscope via a polarization maintaining, single mode optical fibre. A $100\times$ air objective (Olympus, MPlan FL, NA = 0.9) was used. The scattered radiation was focused onto a multi-mode fibre ($50\mu\text{m}$ diameter) and a single monochromator (focal length of 300mm and aperture ratio equal to f/4). The integration time for a single spectrum varied from 0.2–0.3s, and the spectral resolution was equal to 3cm^{-1} (600grooves/mm grating used). The spectrometer was calibrated using the spectrum of a Mercury/Argon atomic emission lamp (WITec). Additionally, standard alignment procedures (single point calibration) were performed before each measurement with the use of the Raman scattering line produced by a silicon sample (520.5rel. cm^{-1}). The sampling density of the results presented here varied from 0.2 to $1.7\mu\text{m}$, while the laser power on the sample was in the range of 5–10mW (intensity in the focus spot). Such power allowed for tissues measurements without photo-damage of any of the measured cells. In selected cases 3D confocal Raman imaging of the tissues was performed by imaging repeatedly the same area at several heights of the sample moving in steps of $0.5\mu\text{m}$ up until a considerable decrease in the signal was observed. The central layer was chosen at the Z-position of the maximal intensity of the Raman signal (see for example Fig. 14.4).

Usually, subsequent to Raman measurements, AFM and IR (sometimes before Raman) measurements were performed for selected samples in the diabetes, cancer metastasis and atherosclerosis models. AFM imaging was done in the AC (equivalent to tapping) mode or PFM (Pulsed Force Mode) with force modulation AFM probes ($k = 2.8\text{N/m}$, WITec) and a step resolution of $0.1\mu\text{m}$. Fluorescence imaging was acquired with an Al-Si Nikon confocal laser scanning system built onto a Nikon inverted microscope Ti-E using a Plan Apo $100\times/1.4$ oil DIC objective. The images were acquired at a resolution of 1024×1024 pixels. Specimens were excited with 405, 488 and 561nm diode lasers.

Histochemical staining of liver tissue sections was performed with Oil Red O (Sigma-Aldrich, St. Louis, MO, USA) according to the following scheme: deionized

water (3 min), 60% isopropanol alcohol (2 min), Oil Red O (30 min) and deionized water (1 min). After the application of listed solutions tissue sections were covered with glycerol gel.

14.2.1.3 Data Processing

Raman data analysis was performed with OpusTM and WITec Project PlusTM 2.10 software. Raman images were generated based on the integrated intensity of marker bands and were calculated without pre-processing. Cluster analysis was carried out after cosmic ray removal and background subtraction (using a polynomial or auto-polynomial function). K-Means Clustering (KMC) results were obtained using the Manhattan method for distance calculation. The number of clusters was determined in order to obtain the best recognition between the clusters. This number depended on the size of the imaged area, sampling density and complexity of the sample. The averaged single spectra extracted from the obtained clusters follow the spectral profile of the assigned components.

For statistical analysis, t-Test or ANOVA were applied using commercial computer software (Origin Pro 9.1, OriginLab). Results are presented as means \pm SEM (standard error of mean). A difference between means was considered significant if $p < 0.05$.

The ImageJ processing program [22] was used to calculate the size of lipid raft aggregates (diabetes) and the elastin fibre area (hypertension).

14.2.2 Results and Discussions

14.2.2.1 Type 2 Diabetes Mellitus (T2DM)

Long standing diabetes leads to structural and functional changes in both the micro- and the macro vasculature system, particularly in the endothelium. To investigate these changes, a multiparameter approach based on the combination of Raman confocal 3D imaging with AFM was applied to analyze alterations in the endothelium in the murine model of diabetes (Fig. 14.3). Leptin-receptor deficient mice (db/db) [23] were used as a model for type 2 diabetes, while heterozygotic db+ mice established the control group. Simultaneous application of Raman and AFM imaging to the same area of the sample enabled obtaining information about both the chemical composition and physical properties of studied tissue fragments in the *en face* preparation [24].

The apparent differences observed in the images of the endothelium of the db/db and db+ mice were related to the presence of the lipid-rich structures at the very top of the studied tissue, i.e. at the uppermost layer of the endothelium. The combination of Raman imaging and AFM was a key point in characterization of these structures, which formed upon the pathology progress. Obviously, these structures

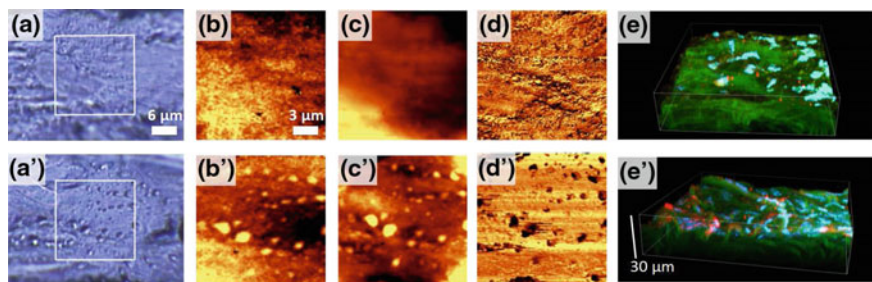


Fig. 14.3 Combined Raman and AFM imaging of *en face* aorta in db/db [diabetic, (a–e)] and db+ [control, (a'–e')] mice: Visual images (a, a'), Raman distribution images obtained by integration of the range 2800–3100 rel. cm^{-1} (b, b'), AFM topography images (c, c'), AFM phase images (d, d') and confocal fluorescence images [(e, e'); endothelial caveolin-1, cell nuclei and elastin fibers visualized in red, blue and green channels] for db+ (a–e) and db/db (a'–e') samples. Figure adapted upon Creative Commons Attribution License from [24]

had an increased lipid content as shown by the enhanced intensity of the band due to the C-H stretching vibrations (2800–3100 rel. cm^{-1} range) in the Raman images of samples from mice with developed diabetes. Topography AFM images indicated that these assemblies were protuberances of the tissue surface, while the phase images demonstrated that they had a considerably different physicochemical character relative to the surroundings. This observation confirmed that these protuberances were localized, above the surface of the tissue and were not deposited below the membrane level. A detailed chemical characterization of the observed lipid-rich structures was undertaken based on the depth profiling of the tissue and subsequent analysis of the recorded spectra with the help of cluster analysis (K-means, Manhattan distance). Figure 14.4 presents the results of the cluster analysis of the single lipid-rich structure [24].

The central part of the structure, extracted as an orange class, exhibited a Raman signature significantly different than the surroundings of the assembly. Generally, the increased intensity of the bands characteristic for lipids (at 1745, 1446–1455, 1300–1315, 1134 and 1075 rel. cm^{-1}) was observed in the average spectrum of this class. In addition, the increase of the intensity of the band at ca. 1099 rel. cm^{-1} , due to the symmetric phosphate stretching mode, and the appearance of two other features: at ca. 780 rel. cm^{-1} , due to the O-P-O bending mode and, particularly, at 725 rel. cm^{-1} , assigned to the symmetric stretching vibrations of the $\text{N}^+(\text{CH}_3)_3$ choline group in sphingolipids [25] was also observed. The chemical characteristic of the lipid-rich assemblies along with the AFM-based information about the localization of these protuberances on the very top of the endothelium enabled identification of these structures as aggregated lipid rafts. Lipid rafts are nanoscale assemblies that may agglomerate into bigger structures upon certain stimuli as described in [26]. A way of initiation of this process is, among others, cross-linking of lipid raft proteins with the cholera toxin or anti-caveolin-1 antibody, a method enabling fluorescent detection of caveolin-1, the raft characteristic protein [27]. Fluorescence microscopy is the main

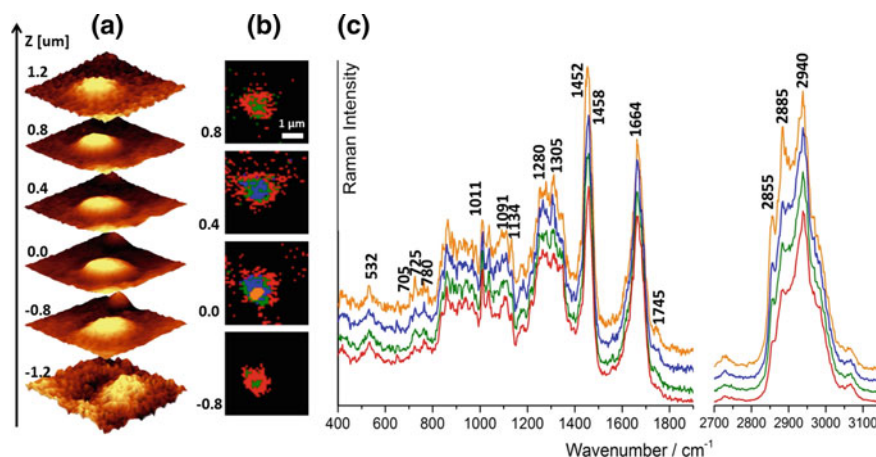


Fig. 14.4 Depth profiling of the aggregated lipid raft: Raman distribution images (integration over the band in the 2800–3100 rel. cm^{-1} range) at different depths [denoted by Z value, the layer marked as $Z = 0.0\mu\text{m}$ was chosen by maximizing the Raman intensity signal, (a)], Cluster Analysis of the corresponding images (b) with the averaged spectra of the clusters [(c), spectra were normalized to the 1011 rel. cm^{-1} band and offset in order to emphasize the differences between them. The Raman intensity in the 2700–3200 rel. cm^{-1} range is 3.5-fold relatively to the fingerprint region]. Figure adapted upon Creative Commons Attribution License from [24]

method used to study lipids rafts and it was used also to confirm the Raman and AFM based observations (Fig. 14.3e, e'). In agreement with the results of Raman-AFM imaging, fluorescence images also demonstrated a significant increase in the number and size of lipid rafts aggregates in the endothelium of the db/db mice compared with the control ones. Nevertheless, fluorescence detection of rafts possesses the inherent problem related to the above-mentioned label-induced aggregation [27]. Therefore, the label-free methodology based on subsequent Raman and AFM imaging, has the advantage of registration of unperturbed and size-conserved lipid rafts assemblies. The benefit of this approach is the possibility of the estimation of the size of formed aggregates. AFM is the method of significantly better spatial resolution relative to confocal Raman microscopy, therefore, obtained AFM topography images were used to calculate the height and the x,y dimensions of lipid rafts aggregates (Fig. 14.5a).

The size of the observed lipid rafts assemblies spanned the range of 300–3000nm in x, y and ca.30–300nm in z. It was also noticed comparing 16- and 20-weeks old mice that with pathology development the size (particularly the height) of lipid raft aggregates increased due to progressive clustering of rafts into bigger platforms [24]. Additionally, interrelation of Raman and AFM-based data enabled to correlate the lipid content in the lipid raft aggregates with their size (Fig. 14.5b). The overall lipid content, measured as the ratio of the integral intensity of the band characteristic for lipids and proteins at ca. 2940 rel. cm^{-1} to the band due to phenylalanine at $\sim 1005\text{rel. cm}^{-1}$, increased with the increase of the area of rafts. The increase of the lipid character of lipid rafts with the size (and therefore the disease progression)

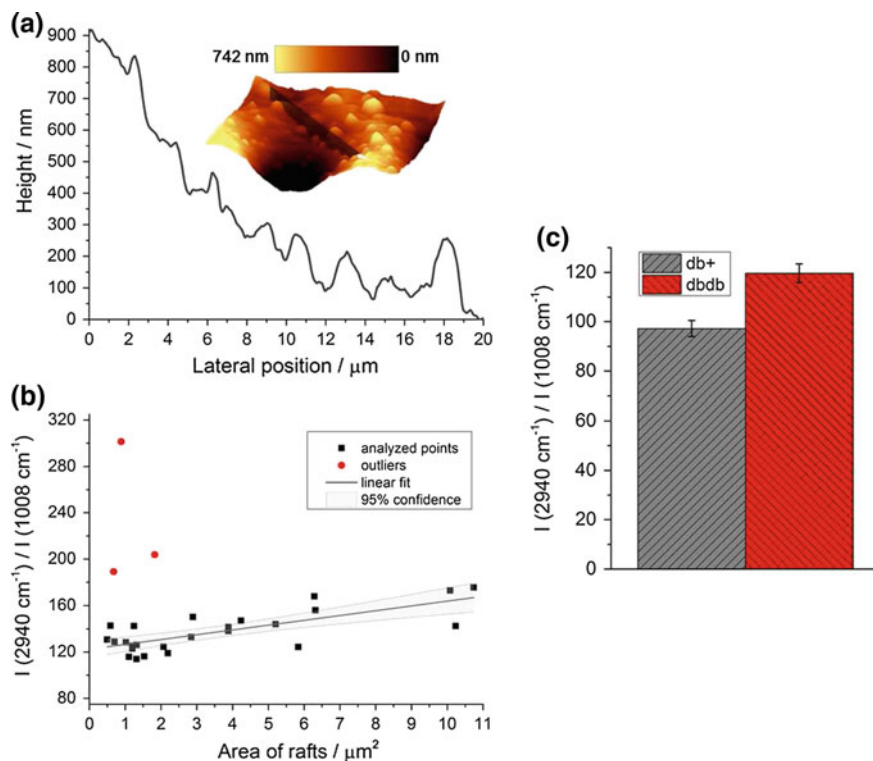


Fig. 14.5 The size and lipid content of lipid raft aggregates in endothelium upon diabetes development: A representative AFM topography image with the cross-section showing the height of lipid aggregates (a), correlation of the rafts area and their relative lipid content (b) and comparison of the average lipid content in the db+ and db/db tissue (c). Figure adapted upon Creative Commons Attribution License from [24]

resulted in one more pattern, i.e. the overall increase of the lipid content in the tissue upon T2DM development, observed in the average Raman spectra of tissue as the increase in the intensity of the band at ca. $2940 \text{ rel. cm}^{-1}$ to the feature at $\sim 1005 \text{ rel. cm}^{-1}$. The increase of the overall lipid content in the tissue is, therefore, caused by aggregation of lipid rafts in the endothelium resulting in about ten-fold increase of the lipid rafts coverage of endothelium surface.

It is important to underline that elucidation of the pathological mechanism associated with lipid rafts aggregation was possible due to the application of the methodology based on the combined confocal Raman imaging and AFM. Raman data enabled a detailed chemical characteristics of lipid rafts, while AFM topography images demonstrated the localization of these structures. Additionally, phase AFM images served as proof that the observed structures coated the endothelium i.e. they were not covered with the cellular membrane as for example lipid droplets. Additionally, the AFM images enabled determination of the size of lipid rafts aggregates. Interrelation

of Raman and AFM data that resulted in correlation of the size of rafts with their chemical composition showed that lipid character increased with the increased size of the aggregates [24].

14.2.2.2 Hypertension

Hypertension, a condition of elevated blood pressure, is associated with the vascular stiffness, endothelial dysfunction and abnormalities in nitric oxide (NO) production pathway [28, 29]. To evaluate endothelial changes upon hypertension development three groups of animals were studied: control mice (C57BL/6J), animals supplemented with L-nitroarginine methyl ester (L-NAME, 8 weeks treatment; 100mg kg⁻¹) and, to evaluate efficiency of treatment, NO-deficient mice supplemented with nitrate (8 weeks treatment; 100mg kg⁻¹ + NaNO₃ in a dose of 1mmol kg⁻¹) [30]. Representative Raman images of aorta cross-sections for these three groups of animals are shown in Fig. 14.6a–c.

No apparent differences were observed in the Raman distribution images of vessel wall cross-sections in the three groups of animals studied. Additionally, as the boundary between the *tunica intima* and *media* was not clear, separation of the signal from the endothelium was impossible based on these images. Therefore, multivariate data analysis was applied to extract the endothelial layer observed in Fig. 14.6 (column 4)

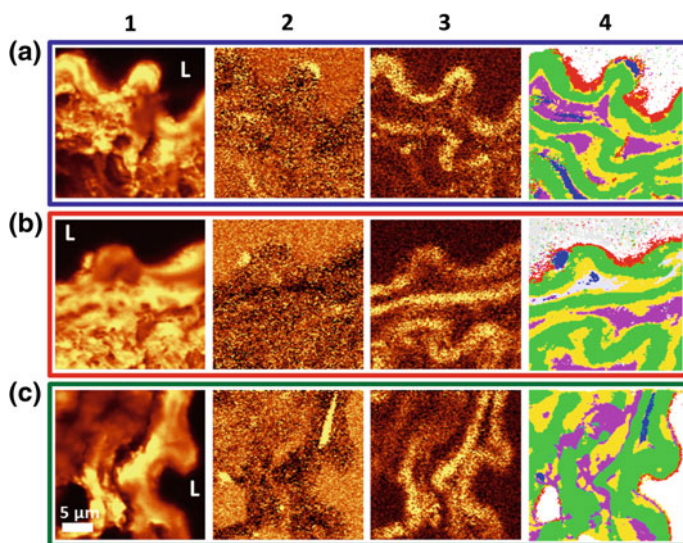
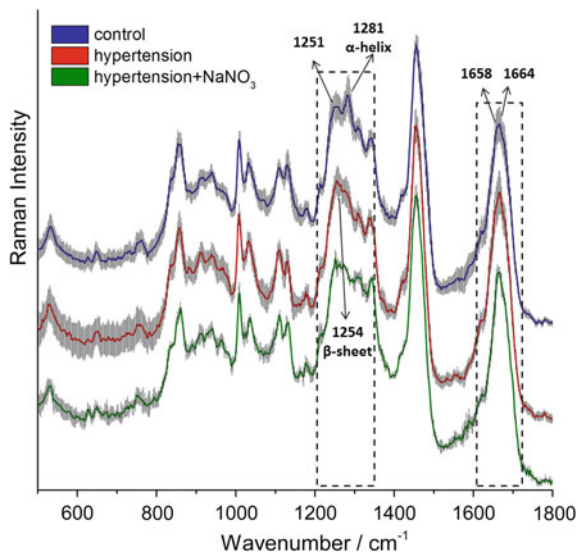


Fig. 14.6 Representative images of aorta cross-sections in control (row a), NO-deficient (row b) and NO-deficient nitrate-treated (row c) mice: Raman images showing distribution of organic matter (column 1, integration in the 3100–2800 rel. cm⁻¹ range), cell nuclei (column 2, integration in the 775–800 rel. cm⁻¹ range) and elastin fibers (column 3, integration in the 540–560 rel. cm⁻¹ range) with cluster analysis images (K-means, Manhattan distance, column 4)

Fig. 14.7 Comparison of the average endothelium spectra in control, NO-deficient and NO-deficient, nitrate-treated mice: The average spectra of the control (blue: 360 spectra, 7 animals), NO-deficient hypertensive (red: 360 spectra, 7 animals) and nitrate-treated (green: 250 spectra, 3 animals) mice taken from the endothelium region with standard deviation on each data point of the spectra. Adapted from [30] with permission from The Royal Society of Chemistry



as the red class. Extraction of the endothelium signal was verified by the localization of the endothelial nuclei and the internal elastic lamina (Fig. 14.6, column 3 and the green cluster in 4). To determine global changes in the endothelium Raman profile upon hypertension development and nitrate treatment, the representative spectra of the endothelium were obtained by averaging of random spectra extracted from Raman measurements of control, NO-deficient and NO-deficient nitrate-treated groups of mice (Fig. 14.7). Overall, 12 Raman measurements were recorded both for the vessel wall of control and NO-deficient hypertensive mice and 5 for the nitrate-treated hypertensive animals, and 360 and 250 spectra in total were averaged for control/NO-deficient and NO-deficient drug-treated hypertensive mice, respectively.

The average spectra demonstrate chemical alterations occurring in the endothelium upon hypertension development and nitrate treatment (Fig. 14.7). The most evident changes were observed in the 1400–1200 rel. cm^{-1} spectral region (i.e. Amide III region) and were related to changes in the secondary structure of endothelial proteins. Particularly, the decrease in the intensity of the band at 1281 rel. cm^{-1} , assigned predominantly to the α -helix protein structure, and the parallel increase of the intensity of the signal at 1254 rel. cm^{-1} , attributed to the β -sheet, observed in the average spectra of mice with hypertension (both treated and untreated) were indicative of the α to β protein structural conversion. Additionally, analogical changes were seen in the Amide I range. The relative abundance of the band at 1656 rel. cm^{-1} , characteristic for the α -helix (and lipids), decreased from 27 to 22% in favour of the β -sheet counterpart at 1668 rel. cm^{-1} that increased from 25 to 30% [30]. Significantly, none of the above-mentioned alterations were reversible upon treatment, as the spectral profiles of hypertensive and hypertensive drug-treated endothelium were quite alike in the Amide I and III ranges. Previously, structural rearrangement of α -helix to

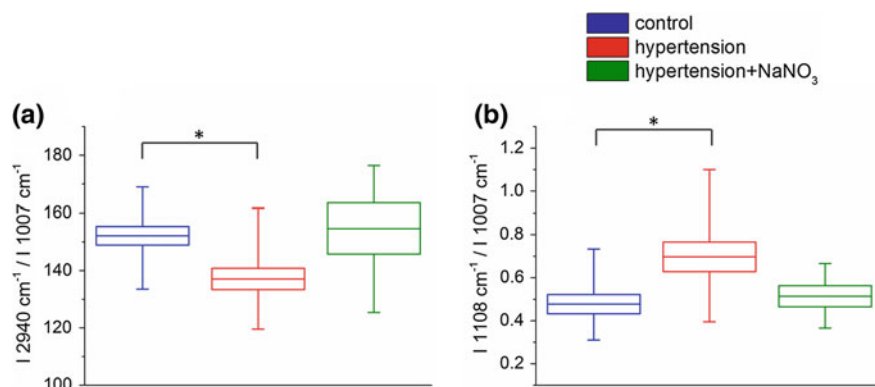


Fig. 14.8 Chemical changes in the murine endothelium upon hypertension and nitrate-treatment. The ratio of the integral intensity of bands at 2940/1005 rel. cm^{-1} (a) and 1108/1005 rel. cm^{-1} (b) in the endothelium of control (blue box), NO-deficient hypertensive (red box) and NO-deficient drug-treated mice (green box). Boxes, lines and whiskers denote standard error, mean and max/min values, respectively; *, $p < 0.05$

the β -sheet have been observed upon melanoma skin cancer [31] and diabetes [32] development.

As the lipid and protein relative content is an important marker of the pathological changes in the tissues, the relative lipid to protein ratio was calculated for the average spectra of the endothelium in three studied groups of mice based on the integral intensity of the band for lipids and proteins centered at 2940 rel. cm^{-1} and the phenylalanine band at $\sim 1005 \text{ rel. cm}^{-1}$. The resulting ratio (Fig. 14.8a) demonstrated that hypertension resulted in the statistically significant increase of the lipid content relatively to the protein content in the endothelium.

This chemical change, contrarily to the previously described rearrangement of the secondary protein structure, was fully reversible upon treatment as the lipid to protein level increased up to the level in control upon nitrate supplementation of the NO-deficient hypertensive animals. Additionally, the change in the relative intensity of the band at 1108 rel. cm^{-1} was observed as shown in Fig. 14.8b. This band is assigned to the twisting vibrations of the NH_2 group [33] and very often assigned to desmosine and isodesmosine [34], amino acids characteristic for elastin structure. The proposed explanation for the increase of the intensity of the band at 1108 rel. cm^{-1} relatively to the band at $\sim 1005 \text{ rel. cm}^{-1}$ was the increased production of elastin-forming amino acids (desmosine and isodesmosine) in the endothelium upon pathology development. Alterations related to the band at 1108 rel. cm^{-1} were also reversible upon treatment.

Investigation of cross-sections of aorta enabled determining changes not only in the endothelium, but also in the deeper layers of the tissue sample. Vascular remodeling of the vessel wall, manifested as thickening of the elastin fibers was clearly seen in the Raman images of *tunica media* of animals with hypertension (both treated and untreated, Fig. 14.9), in agreement with previous reports [35].

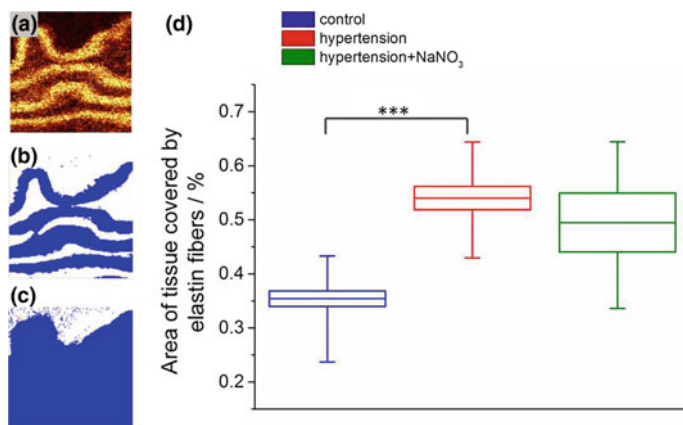


Fig. 14.9 Hypertension-induced changes in *tunica media*: A Raman image of elastin fibers (integration in the 540–560 rel. cm^{-1} range, **a**) in the vessel wall of the control mice and the images showing methodology of calculating the elastin thickness: images showing the area covered by elastin (**b**) versus tissue area (**c**) and the calculated tissue area covered by elastin fibers for control, NO-deficient and NO-deficient nitrate-treated mice (**d**). Boxes, lines and whiskers denote standard error, mean and max/min values, respectively; * * *, $p < 0.005$

Various structural (the relative increase of the β -sheet content versus the α -helix, thickening of elastin fibers in *tunica media*) and chemical (the relative decrease of lipid-to-protein ratio and increase of the content of the elastin-forming amino acids) changes associated with the development of hypertension were characterized in the vessel wall based on Raman imaging. Additionally, the efficacy of the nitrate supplementation on hypertension development in the vessel wall was assessed, showing that chemical, but not structural alterations in the vessel wall can be reversed upon nitrate supplementation.

14.2.2.3 Cancer Metastasis

Molecular specificity in conjunction with chemometric methods of data analysis makes Raman spectroscopy a potent tool to recognize precancerous or early cancerous changes in tissues [36–38], but not too much attention was devoted to study metastasis processes with the help of this technique. It has been recently reported that the endothelium, being a barrier for migrating cancer cells, undergoes significant alterations upon cancer metastasis [39–41]. To investigate these changes, the combined Raman and AFM imaging of the *en face* vessel wall of BALB/c mice (7–8 weeks old females, Charles River Laboratories) orthotopically inoculated with viable 4T1 tumor cells (American Type Culture Collection) and healthy BALB/c mice was performed [7]. In order to extract the signal from the endothelium, Raman imaging was repeated for several layers of the sample, starting from the layer of the maximum signal and going up every $0.5\mu\text{m}$ up to the layer where the Raman

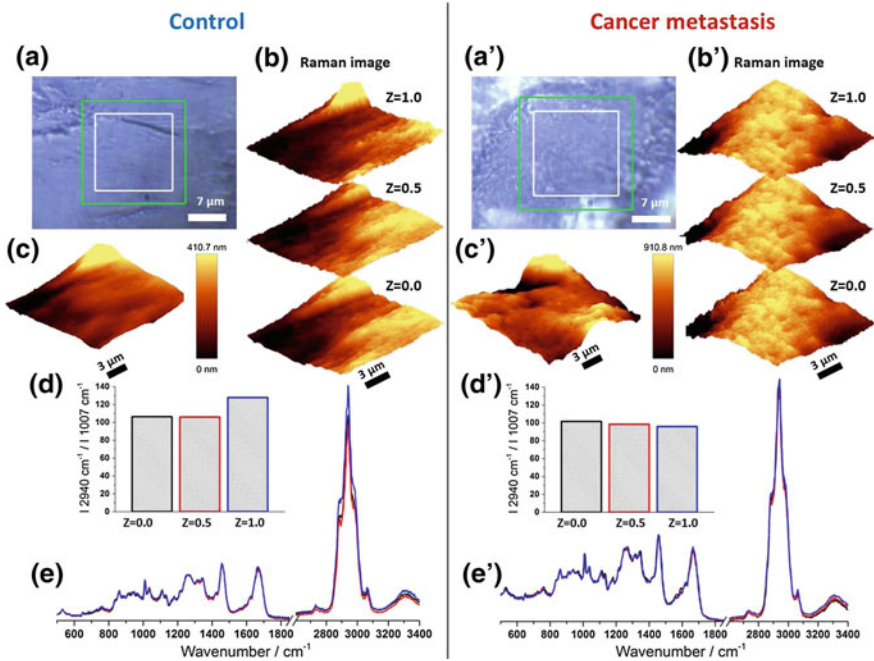


Fig. 14.10 Results of representative measurements of the vessel wall in control (left panel) and upon cancer metastasis (right panel): The areas of Raman and AFM measurements are denoted with white and green rectangles, respectively, in the visual images (**a**, **a'**). Three Raman distribution images at different depths of tissue were obtained by integration of the band in the range of 2800–3100 rel. cm^{-1} (**b**, **b'**) and compared with the AFM topography images (**c**, **c'**). The lipid to protein ratio (**d**, **d'**), defined as the intensity ratio of the band at 2940 rel. cm^{-1} to the band at $\sim 1005 \text{ rel. cm}^{-1}$, was calculated based on the average spectra (**e**, **e'**) of presented Raman images (**b**, **b'**). Figure adapted upon Creative Commons Attribution License from [7]

signal was unmeasurably low. Raman measurements were complemented with the AFM imaging, applied to confirm approximate flatness of the surfaces, necessary for effective separation of the signal from different layers. Finally, Raman spectra recorded for different layers were analyzed separately by averaging of all spectra belonging to a given layer. A representative set of data for control and metastatic tissues (Fig. 14.10) demonstrated that the chemical composition of the endothelium of mice with cancer metastasis was significantly different compared to the endothelium of the control group.

The most prominent differences in the tissues of control and metastatic mice were related to the overall lipid and protein content calculated based on the integral intensity of the signals at ca. 2940 rel. cm^{-1} and $\sim 1005 \text{ rel. cm}^{-1}$, respectively. In particular, the vascular endothelium of the control mice has the higher content of lipids and/or the lower content of the proteins than the deeper layers of the aorta. This effect is not observed for the tissues of metastatic animals, where the lipid to protein

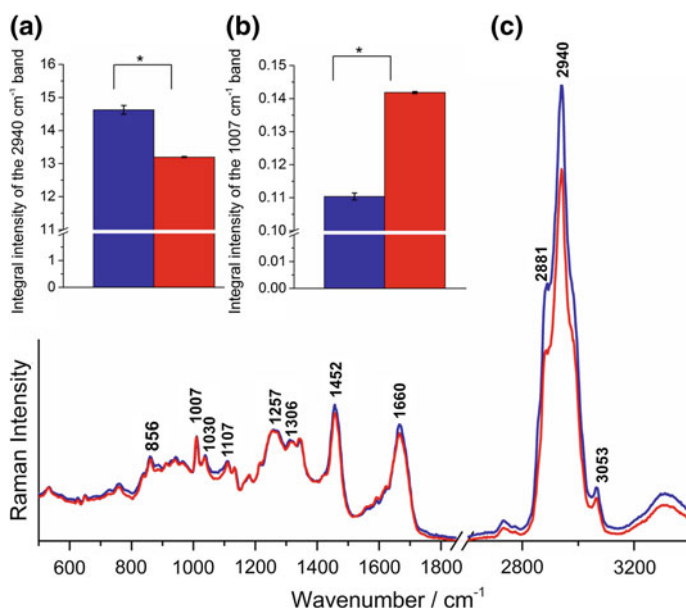


Fig. 14.11 Lipid and protein content in the endothelium of control and metastatic mice: The integral intensity of the lipid (a) and protein (b) bands and the comparison of the average endothelium spectra (c): control (blue), and metastasis-altered (red, spectra were normalized to the phenylalanine band at $\sim 1005 \text{ rel. cm}^{-1}$). Figure adapted upon Creative Commons Attribution License from [7]

ratio is comparable for all measured layers. Moreover, for deeper layers of the tissue, the lipid-to-protein ratio for metastatic and control mice is comparable, showing that the effect of a changed lipid-to-protein ratio is confined to the endothelium. To answer the question which of the components i.e. lipids or proteins change its content upon metastasis, vector normalization of the average spectra (in the $3200\text{--}450 \text{ rel. cm}^{-1}$ range) and calculations of the integral intensity of the following bands: $2940 \text{ rel. cm}^{-1}$ (in the $3030\text{--}2825 \text{ rel. cm}^{-1}$ range) and $\sim 1005 \text{ rel. cm}^{-1}$ (in the $1023\text{--}993 \text{ rel. cm}^{-1}$ range) were performed (Fig. 14.11).

The results demonstrate that the lipid content significantly (about 6%) decreased for the metastatic mice relatively to the control ($p = 0.013$), while even more striking effect of the metastasis was observed for proteins. The intensity of the band at $\sim 1005 \text{ rel. cm}^{-1}$ increased up to 22% ($p = 0.011$) in the endothelium upon metastasis in comparison with the control. The phenotype of “cancer associated” dysfunctional endothelial cells has been previously characterized in vitro showing that these cells were more active, e.g. secreted larger amounts of proteins (mainly pro-inflammatory cytokines) [39]. This finding is in agreement with changes in the protein and lipid content observed in Raman spectra of the endothelium upon metastasis resulting from dysfunctional activation related to cancer and inflammation mediators.

The endothelium-confined chemical changes upon cancer metastasis were detected due to application of the 3D confocal imaging and analysis of the information from

the consecutive layers individually. Metastasis-induced changes in the endothelium are one more example of a critical role of endothelial response to various pathologies related not only topically to the vessel wall, but also via the systemic inflammation [7].

14.2.2.4 Atherosclerotic Plaque

The consequence of the atherosclerosis disease is the formation of the plaque inside arteries. In the advanced stage of atherosclerosis the plaque may contain calcified lesions with inflammatory cells and lipids what hardens and narrows arteries. A detailed review of the research on atherosclerotic plaque with the use of Raman spectroscopy was previously published [42]. It has been also shown that Raman spectroscopy offers high content images (micro and sub-micro resolution) of the morphological structure of the tissue of diagnostic, prognostic and therapeutic significance [43].

The use of Raman imaging in studies of the cross-sections of the atherosclerotic plaques in different murine models allowed us for biochemical analysis and visualization of the most important plaque features. Micro-damages of the fibrous cap, the exact places where the cholesterol crystals are created, the distribution of calcification and many other aspects visualized by Raman microscopy provide additional knowledge compared to just quantitative measurements of an average plaque features in some parts of aorta. This helped us to study the atherosclerosis progression, impact of different diets on plaque formation, its distribution as well as its vulnerability.

Figure 14.12 shows the Raman images of selected areas of the cross-section of plaques from a brachiocephalic artery (BCA). Distribution of the organic matter was obtained by integration of the CH stretching band approx. in the region 2800–3020 cm^{-1} . The use of a 532nm excitation induced not only Raman effect, but also autofluorescence of the sample. Autofluorescence of internal elastic lamina and fibrous cap (called generally “elastin”) manifested itself by an increased background. The increased background can be also associated with hemoglobin (Hb), which absorbs a considerable amount of photons [45]. The KMC results show four main clusters of the plaque: lipids, remodelled media, heme and elastin. Taking into account the place of deposition of heme, in both plaques we can observe intraplaque hemorrhages and only in the second example (e’) the luminal thrombus. The green cluster corresponds mainly to internal elastic lamina of the artery wall, however in both examples we can also see the fibrous cap. The average spectra of the respective four clusters of the tissue and comparison with IR and AFM results are discussed in [44].

Raman imaging of the selected areas of the plaque was successfully used in combination with IR studies to characterize biochemical content of BCA plaques from ApoE/LDLR^{-/-} mice fed Low Carbohydrate High Protein (LCHP) diet as compared to American Institute of Nutrition (AIN) diet. High resolution Raman imaging enabled the identification of necrotic core/foam cells, lipids (including cholesterol crystals), calcium mineralization and fibrous cap. Raman imaging was particularly

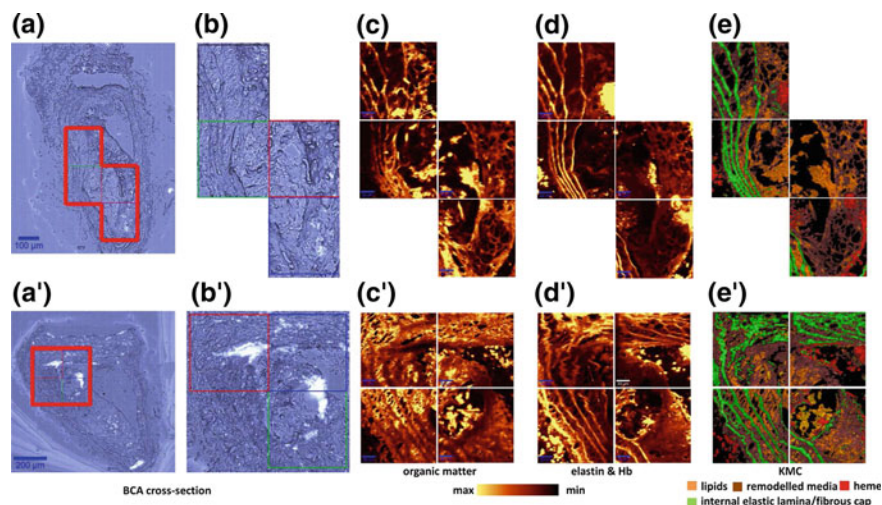


Fig. 14.12 Raman images obtained from the selected areas of the cross-section of atherosclerotic plaques obtained from BCA: (a, a') microphotographs of the cross sections of a brachiocephalic artery taken from a 6-month-old ApoE/LDLR^{-/-} mouse fed chow diet with the labelled areas (b, b') investigated with the use of Raman; (c, c') Raman images obtained by integration of the CH stretching band in the region 2800–3020 rel. cm⁻¹; (d, d') Autofluorescence images of samples connected with the presence of elastin features (internal elastic lamina and fibrous cap and hemoglobin); (e, e') KMC results with four main clusters which include remodelled media, heme, internal elastic lamina/fibrous cap and lipids. Sampling density was equal to 1.7 μm. Adapted with permission from [44]. Copyright (2014) WILEY-VCH Verlag GmbH & Co. KGaA

useful to describe the relative thickness of the outer fibrous cap and the presence of buried caps, which are known to be prominent features of the vulnerable plaques [46].

Figure 14.13 shows a high resolution (sampling density equal to 0.33 μm) imaging of the luminal part of the calcified plaque. The presence of the fibrous cap, which separates the plaque from the artery lumen, can still be observed. The occurrence of small amounts of heme on top of the fibrous cap corresponds rather to free heme from destroyed red blood cells than to a luminal thrombus. The interior part of the plaque is occupied by calcification and lipids. The average Raman spectra of the elastin-rich cluster (fibrous cap/internal elastic lamina) are characterized by the bands related to proteins in general, i.e. Amide I at 1660 rel. cm⁻¹, Amide III approx. at 1257 rel. cm⁻¹ and phenylalanine at ~1005 rel. cm⁻¹ as well as bands specific for desmosine, isodesmosine (1108, 1336 rel. cm⁻¹) and disulphide bridges in elastin (530 rel. cm⁻¹). The use of the 532nm excitation gives the resonance Raman (RR) spectrum of Hb (heme class) with the strongest bands at around 1580, 1130 and 750 rel. cm⁻¹. These bands originate from the ν_{19} , ν_{22} and ν_{15} modes, respectively. The Raman spectrum of calcified lesion is characterized by the intense band at approx. 960 rel. cm⁻¹, which is assigned to the stretching vibrations of $\nu(\text{PO}_4)$. Other bands of hydroxyapatite are observed at 440, 590 and 1081 rel. cm⁻¹. Because the Raman

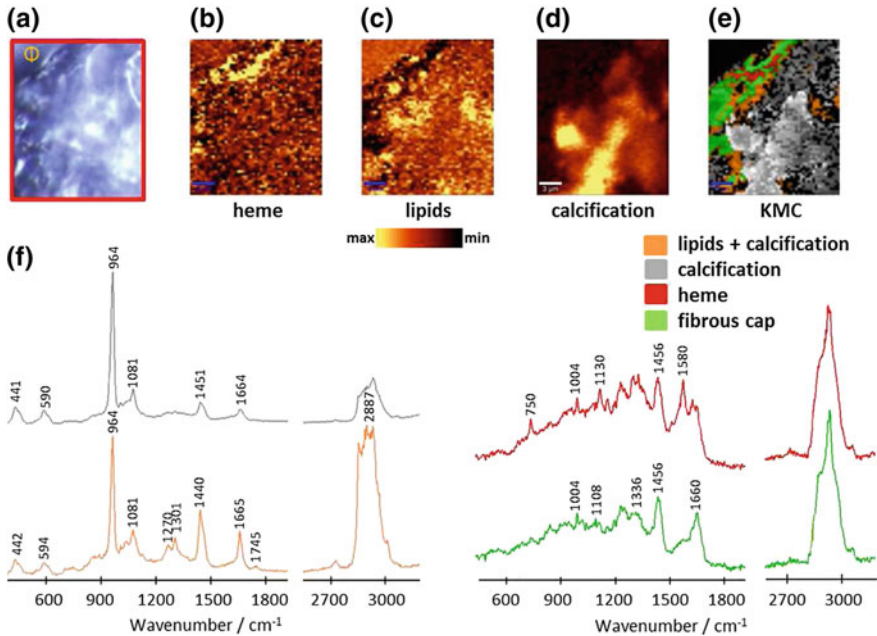


Fig. 14.13 Raman results from the calcified plaque: **a** Microphotograph of the cross section of a brachiocephalic artery taken from a 6-month-old ApoE/LDLR^{-/-} mouse fed chow diet with the labeled area (red) investigated with the use of Raman spectroscopy; Raman distribution images obtained by integration of **b** hemoglobin (heme) band at 1580 rel. cm^{-1} and **c** lipid band at 2887 rel. cm^{-1} and **d** hydroxyapatite band at 964 rel. cm^{-1} ; **e** KMC results with the four main clusters, which include heme, fibrous cap, calcification and lipids; **f** The average spectra of heme, fibrous cap, calcification and hydroxyapatite mixed with lipids obtained from whole measured tissue. The Greek letter “ Φ ” indicates the side of artery lumen

spectrum in Fig. 14.13 corresponds to the lipid cluster mixed with the calcified lesion, we may suspect that this plaque comes from the mice with the advanced stage of atherosclerosis. The bands typical for lipids maybe observed at around 1745 rel. cm^{-1} (C=O stretching mode), 1670 rel. cm^{-1} (C=C stretching mode) and 1440 rel. cm^{-1} (C-H bending mode), however the most intense bands are visible in the higher wavenumber region, and originate from the stretching vibrations of CH groups. Overall, the method enables not only imaging of the total amount of lipids, but sometimes also differentiation of the cholesterol from the cholesteryl esters is also possible (Fig. 14.14).

Differentiation between cholesterol and cholesteryl esters can be made by integration of bands at 1740 or 2887 rel. cm^{-1} , which are characteristic for C=O and C-H stretching vibrations in esters, respectively. Bands observed at lower frequencies, below 700 rel. cm^{-1} are characteristic mainly for cholesterol moiety due to vibration modes of the steroid ring. Single Raman spectra obtained from the cholesterol crystals in the studied plaques may even allow for detection of the specific type of

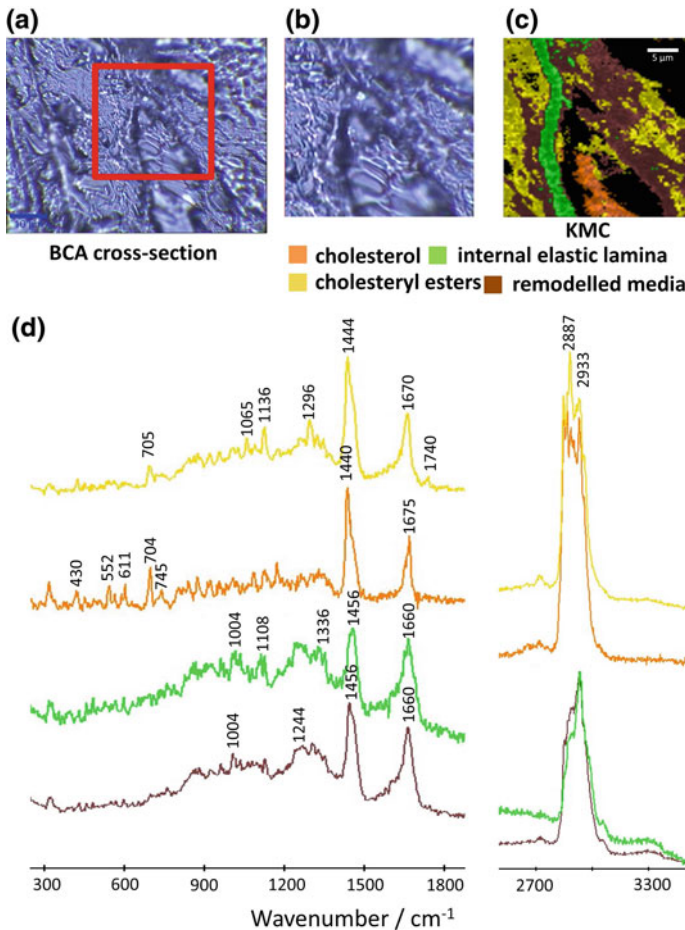


Fig. 14.14 Differentiation between cholesterol and cholesteryl esters inside a plaque: **a** Microphotograph of the cross section of a brachiocephalic artery taken from a 6-month-old ApoE/LDLR^{-/-} mouse fed LCHP diet with the labeled area **b** investigated with the use of Raman spectroscopy; **c** KMC results with four main clusters which include remodelled media, internal elastic lamina and cholesterol esters and cholesterol; **d**. The average spectra of the respective four clusters of the tissue. Sampling density was equal to 0.33 μm

crystalline cholesterol [44]. The Raman spectrum of remodelled media, which corresponds to the pathologically altered media tissue, is very similar to elastin features, but this part of plaque does not exhibit autofluorescence when the 532nm excitation is used. To confirm the legitimacy of Raman results, they were compared with the histopathological staining [42, 44].

Additional information about atherosclerotic plaque may be obtained when confocal Raman imaging is combined with IR imaging or AFM. All these methods can be carried out on the same area of the tissue and can be successfully used in

atherosclerotic plaque analysis [44]. Figure 14.15 presents the results obtained by combination of IR and Raman imaging, which allowed [46] for quantitative (IR) and qualitative (Raman) analysis of the vulnerable plaque.

AFM results supported Raman information about the physical properties of the fibrous cap surrounding the atherosclerotic plaque and internal elastic lamina. They were found to be the stiffest parts of the tissue or plaque (besides calcification and cholesterol crystal) and serve as the tissue or plaque framework. As we previously reported with the use of AFM technique and Raman microscopy, it was possible to define the thickness of the murine fibrous caps [44, 46]. AFM allowed also the visualisation of shape and topography profiles of cholesterol crystals and other plaque features (see Fig. 14.16). Additionally, AFM is able to provide the insight into the mechanical properties of the cap.

Presented results indicated that AFM, IR and Raman imaging might be regarded as complementary methods to histological and immunocytochemical staining to study the properties of atherosclerotic plaque. A variety of staining methods specific for individual plaque features is available, however, it is not possible to use them at the same area of the sample. Raman imaging combined with other methods enables detection of all features during one measurement within the specified tissue area and that is, we believe, the main advantage of the multimodal approach presented here.

Chemical analysis of the tissue of organs like liver, brain and lung carried out with Raman imaging and histochemical staining has previously been reported [47, 48]. Moreover, it was also possible to study the primary atherosclerotic changes at the endothelial cell level [49].

14.2.2.5 NAFLD-Affected Liver

Non-Alcoholic Fatty Liver Disease (NAFLD) is a common chronic liver disorder, considered as a manifestation of metabolic syndrome [50, 51]. It can be characterized as an excessive accumulation of lipids in the liver tissue in the form of LDs. The lack of specific symptoms as well as of optimal diagnostic methods makes the detection of this disorder challenging. If left untreated, NAFLD can lead to liver cirrhosis and fibrosis (Non-Alcoholic Steatohepatitis, NASH) and finally - irreversible liver damage.

For the study of fatty liver various animal models were used. The genetic models involve a mutation in a specific gene, resulting in promoting the development of fatty liver (e.g. spontaneous mutation in the leptin gene in db/db mice). Dietary models are based on selected nutrition protocols, which determine the feeding of animals. They can involve e.g. high content of saturated fats (High Fat Diet, HFD) or deficiency of methionine and choline (Methionine-Choline-Deficient diet, MCD). Finally, the combined models use genetically modified animals fed according to a specific manner (e.g. ApoE/LDLR^{-/-} mice fed with Low Carbohydrate High Protein Diet) [52]. The most commonly used dietary model is the HFD, with the fat content of approx. 60% that includes primarily saturated lipids [53].

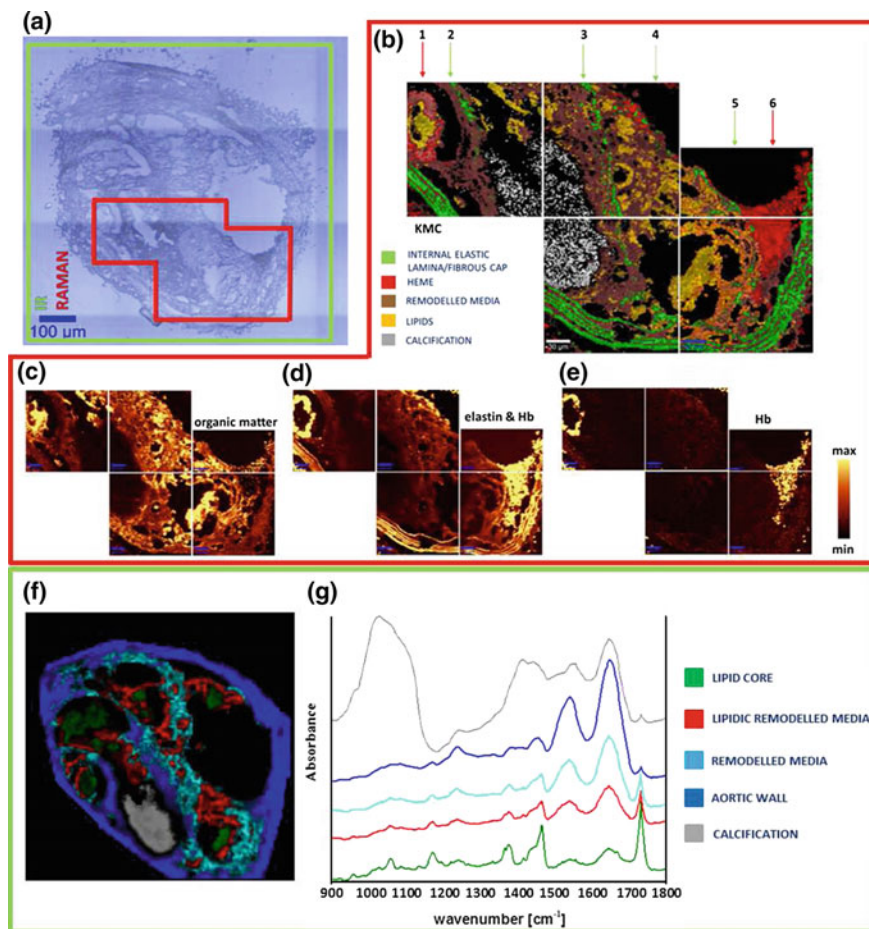


Fig. 14.15 Raman and IR as complementary techniques in plaque studies: **a** Microphotograph of a cross section of a brachiocephalic artery taken from a 6-month-old ApoE/LDLR^{-/-} mouse fed LCHP diet with the labelled regions investigated with the use of IR (green) and Raman (red); **b** KMC results with four main clusters including remodeled media, heme, internal elastic lamina/fibrous cap and lipids; Existence of three buried fibrous caps marked with the green arrows 2, 3 and 5 from the middle to the external part of the plaque, respectively **c** Raman images obtained by integration of the CH stretching band approx. in the 2800–3050 rel. cm⁻¹ region; **d** Autofluorescence of the sample connected with the presence of elastin features (internal elastic lamina and fibrous cap) and Hb; **e** Raman images obtained by integration of the band centered at 1130 rel. cm⁻¹ or 745 rel. cm⁻¹ (Hb); For Raman imaging the sampling density was equal to 1.67 μm. Color coding for the clusters is presented in figure; **f** A Fuzzy C-Means (FCM) clustering image of the whole section, based on FT-IR imaging data, with five clusters. **g** The corresponding average spectra from FCM analysis - spectra were offset for clarity. Figure adapted upon Creative Commons Attribution License from [46]

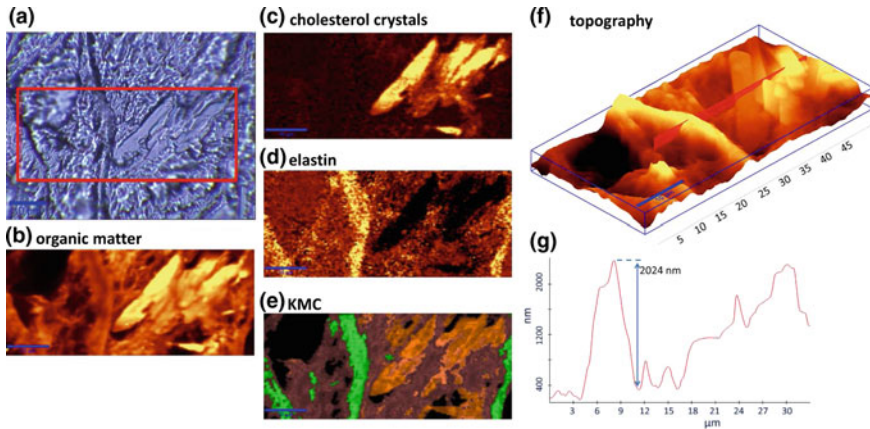


Fig. 14.16 Raman and AFM as complementary techniques in plaque studies: **a** Microphotographs of the cross sections of a brachiocephalic artery taken from a 6-month-old ApoE/LDLR^{-/-} mouse with investigated areas labeled (red). Raman images of: **b** the band due to the CH stretchings approx. in the region 2800–3020 rel. cm⁻¹, **c** cholesterol at 704 rel. cm⁻¹; **d** elastin at 530 rel. cm⁻¹; **e** the KMC results with three main clusters. The clusters include crystalline cholesterol, remodelled media and internal elastic lamina; sampling densities were equal to 500nm; AFM image of: **f** topography of part “a” with the **g** topography cross section according to red line. Adapted with permission from [44]. Copyright (2014) WILEY-VCH Verlag GmbH & Co. KGaA

For the measurements, Raman imaging combined with FT-IR imaging and histochemical staining (considered as a ‘gold standard’) were applied. By performing the experiments with the use of confocal Raman imaging the chemical information can be linked with the spatial information. The location of changes can indicate the type of the liver cell involved in the disease development. Furthermore, Raman imaging allows obtaining detailed information on the molecular level, including the secondary structure of proteins or lipids composition (free fatty acids, triglycerides, cholesterol esters, etc.) [44], as well as it provides information on the location and the structure (a degree of unsaturation, lipid chain branching, etc.) [45, 47, 54].

One of the most prominent features of NAFLD-affected tissue is the presence of relatively large lipid droplets. A comparison between the lipid distribution in livers of C576BL/6J (control) mice fed with AIN-93G (a standard dietary protocol for early growth and reproduction) and HFD (containing 60% of kcal from saturated fat) after 15 weeks is presented in Fig. 14.17.

A distribution of selected components of liver tissue in the control and NAFLD-affected one (Fig. 14.17) distinctly reveals the most significant feature of fatty liver: the presence of large lipid droplets [45]. This prominent attribute is connected not only to fatty liver itself, but also to any NAFLD-related diseases, such as atherosclerosis or diabetes mellitus type II [47]. Within healthy tissue small lipid accumulations can sometimes also be observed. They are mainly associated with the storage of vitamin A [45]. However, the size and density of LDs in fatty liver increase drastically,

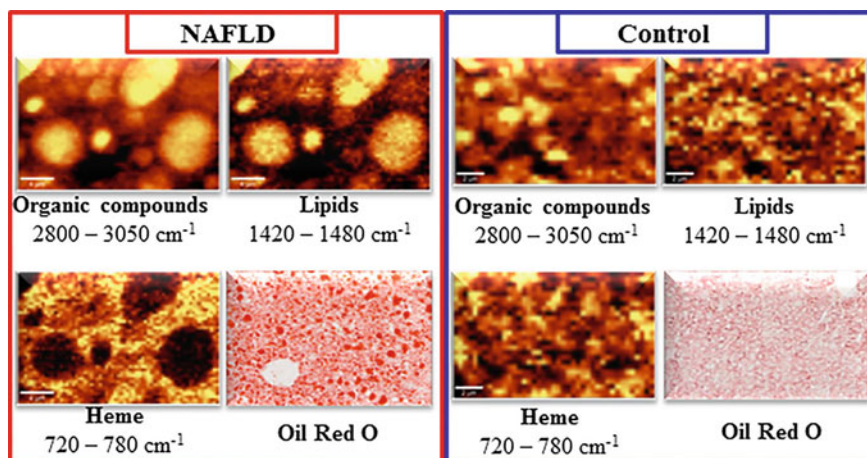


Fig. 14.17 Raman images of liver tissue collected from murine models of NAFLD (red panel) and control (blue panel) along with results of Oil Red O staining: Distribution of organic components ($2800\text{--}3050\text{rel. cm}^{-1}$), lipids ($1420\text{--}1480\text{rel. cm}^{-1}$) and heme ($720\text{--}780\text{rel. cm}^{-1}$). The presence of large lipid droplets within NAFLD-affected tissue can be seen (red panel)

changing the biochemical composition of the tissue entirely and thereby impairing the actions of this organ.

Figure 14.18 shows the results on the composition of LDs. As can be seen the area corresponding to lipid droplets (Fig. 14.18b) is easily identified by KCA due to the significant changes in the collected spectra. However, further analysis of the lipid droplet cluster (Fig. 14.18c) does not reveal any prominent differences. The cluster division is a result of differential intensities of the signals, which decreases from the border of droplet towards its centre. No heterogenic distribution of any lipids in the plane of the droplet can be seen [55]. Confocal Raman imaging allowed additionally investigation of the droplet composition within their volume (Fig. 14.18a), confirming the homogenous distribution of lipids. Interestingly, we were able to observe and to study not only the droplets visible from the surface of the tissue sections but also droplets occurring inside (Fig. 14.18d). Such droplets are exposed to a lesser extent to possible changes in the composition due to preparation or storage of the samples (e.g. changes in the degree of unsaturation due to long exposure to visible light). Their composition is the same as the droplets located on the tissue surface, confirming the proper approach used for the tissue preparation and its storage.

Inspection of the LDs spectra led to the conclusion that the droplets are composed mainly of triglycerides, whereas cholesterol and its esters were not observed. Raman results were confirmed by an assessment of lipid content in the tissue with the use of gas chromatography/mass spectrometry (GC/MS) [56].

A degree of lipid unsaturation can be determined on the basis of the ratio of intensities of bands corresponding to the vibrations of $\text{C}=\text{C}$ and $\text{C}-\text{C}$ moieties, respectively. In Raman spectra of lipids three major bands due to $\text{C}-\text{C}$ vibrations can be iden-

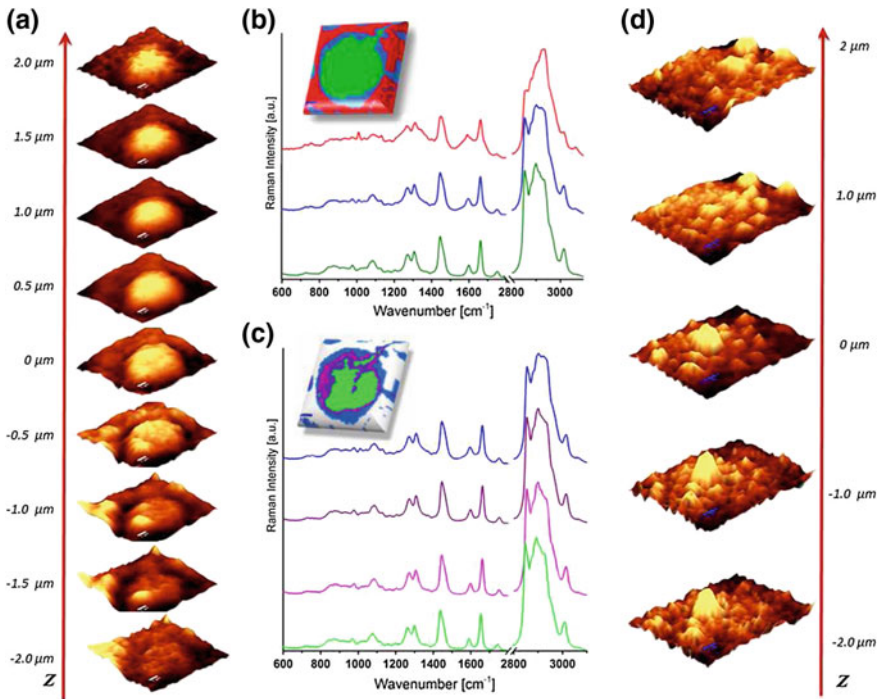


Fig. 14.18 Investigation of LDs composition: **a** A 3D stack representing the distribution of saturated lipids ($1420\text{--}1480\text{ rel. cm}^{-1}$) in lipid droplet from NAFLD-affected tissue (droplet visible on the surface); **b** KMC analysis of LD: the distribution of clusters along with corresponding spectra; **c** KMC detailed analysis of clusters from panel B corresponding to lipid droplet: the distribution of clusters along with corresponding spectra, **d** 3D stack representing the distribution of saturated lipids ($1420\text{--}1480\text{ rel. cm}^{-1}$) in lipid droplet from NAFLD-affected tissue: please notice the location of the droplet deep within the tissue

tified: $\sim 1300\text{ rel. cm}^{-1}$ associated with the CH_2 twisting mode, $\sim 1444\text{ rel. cm}^{-1}$ due to the CH_2 deformation mode and $\sim 2855\text{ rel. cm}^{-1}$ originating from the CH_2 stretching vibrations. Presence of lipids with $\text{C}=\text{C}$ double bonds manifests itself by three major bands: $\sim 1266\text{ rel. cm}^{-1}$ associated with deformation of the $=\text{C}\text{--}\text{H}$ groups, $\sim 1656\text{ rel. cm}^{-1}$ due to the $\text{C}=\text{C}$ stretching and $\sim 3010\text{ rel. cm}^{-1}$ originating from the $=\text{CH}$ stretching vibrations. Therefore, determination of the degree of unsaturation can be performed on the basis of at least three band pairs: I_{3010}/I_{2855} , I_{1656}/I_{1444} and I_{1266}/I_{1301} [55]. The first criterion has, however, a low sensitivity for changes, as the band corresponding to unsaturated bonds is characterized by small intensity compared to the band corresponding to single bond vibrations. Therefore only big changes in the intensity of the band $\sim 3010\text{ rel. cm}^{-1}$ will result in slight changes of the value of I_{3010}/I_{2855} . The criterion of I_{1266}/I_{1301} has been commonly used. However, in terms of biological materials, often characterized by raised baseline and the richness of composition, it is a source of numerous difficulties. The elevated baseline

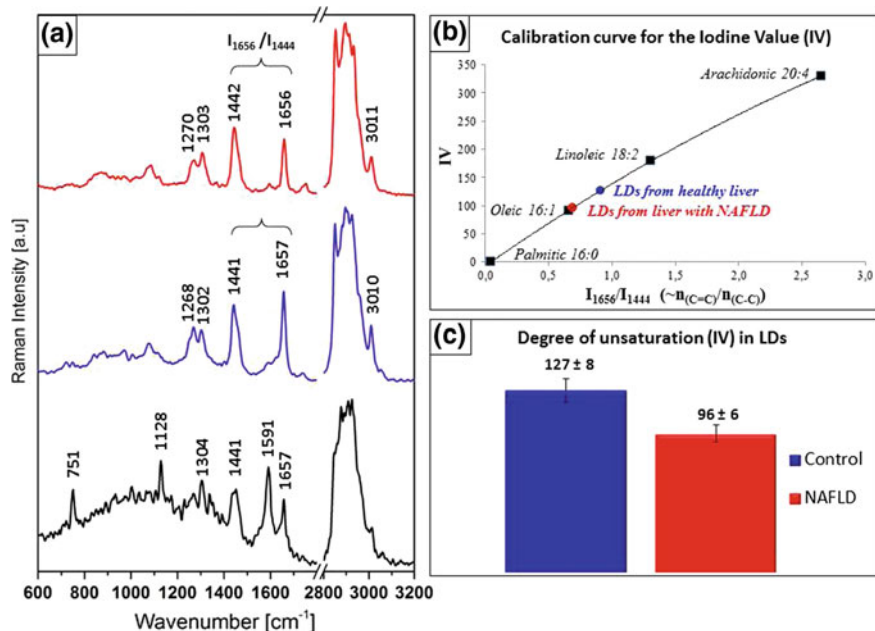


Fig. 14.19 **a** Raman spectra of lipids from NAFLD-affected liver (red), small lipids from control liver (blue) and typical control liver tissue (black); **b** Calibration curve for assessment of iodine value (IV) on the basis of I_{1656}/I_{1444} : red and blue dots mark the values obtained for lipids from control and NAFLD-affected liver; **c** Iodine values (degree of unsaturation) for lipids from control mice and mice with NAFLD. IVs were calculated on the basis of Raman spectra and the calibration curve

is an important problem particularly for the liver tissue, as it is rich in heme. So, the criterion of I_{1656}/I_{1444} seems to be the most suitable for the determination of the degree of unsaturation of lipids in biological materials [54].

A comparison between the degree of unsaturation of lipids from lipids in the liver of control and NAFLD-affected mice indicates a significant difference in their composition (Fig. 14.19).

By the use of standards of free fatty acids it is possible to calibrate the selected criterion (I_{1656}/I_{1444}) and express the degree of unsaturation as iodine value. The value obtained for the sample refers to the lipid mixture building the droplet. As can be seen, the degree of unsaturation decreases considerably for fatty liver droplets. The lipids resulting from pathological disorder induced by high fat diet (containing high amounts of saturated fat) tend to be composed of saturated lipid [45].

The degree of unsaturation is different not only for healthy and diseased tissues but also in the case of pharmacological treatment, based on two reference drugs: metformin, perindopril, and two NO-donors V-PYRRO/NO and V-PROLI/NO. The major change induced by treatment with reference drugs was a clear reduction of the size and number of lipid droplets. This effect has not been observed for any of the NO-donors. In addition to these changes, for the treatment with metformin and perindopril

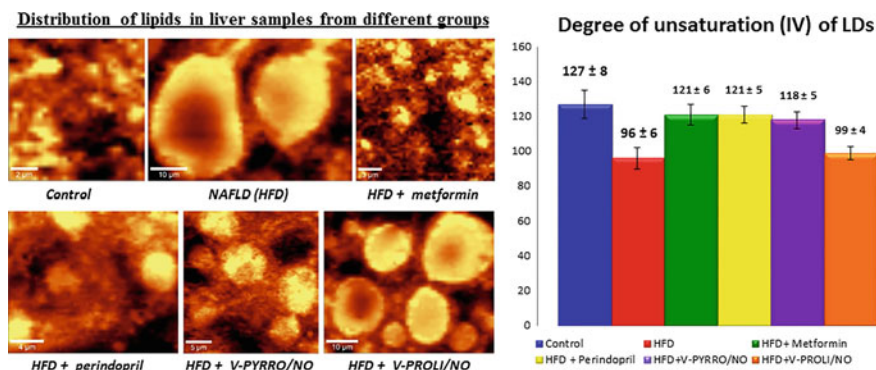


Fig. 14.20 (Left) Distribution of lipids in livers from control, NAFLD (HFD-induced), NAFLD treated with: metformin, perindopril, V-PYRRO/NO and V-PROLI/NO, obtained on the basis of integration of Raman band in the range 1420–1480 rel. cm^{-1} . (Right) Iodine values (degree of unsaturation) for LDs from control mice, mice with NAFLD and mice with NAFLD subjected to treatment. IVs were calculated on the basis of Raman spectra and calibration curve presented in Fig. 14.19b

there was a significant increase in the value of the degree of unsaturation, nearly aligning it with the value determined for control [56]. Therefore, it can be concluded that a successful treatment manifested itself by the change in the composition of LDs and - possibly due to this - the reduction of size and number of LDs.

An interesting observation can be made for the NO-donors (Fig. 14.20). Both of them did not lead to the reduction of the size nor number of LDs. However, an administration of V-PYRRO/NO has resulted in a change of the degree of unsaturation of lipids composing LDs, increasing the iodine value towards the value corresponding to control (similarly as in case of metformin and perindopril). Therefore we can conclude, that the HFD-induced decrease in the ratio of unsaturated (UFA) to saturated fatty acids (SFA) was reversed by treatment with V-PYRRO/NO. GC/MS results confirmed the reduction of the total liver triacylglycerols, diacylglycerols and ceramides fraction. The modification of the composition of LDs (degree of unsaturation) is a change that occurs prior to their size reduction and can indicate the effectiveness of therapy.

The composition of LDs (the ratio of UFA/SFA) depends on many factors, including e.g. diet or type of NAFLD. The dietary model of HFD results in large droplets in the fatty liver. The changes in the degree of unsaturation for the small droplet type model can be tested using ApoE/LDLR^{-/-} mice fed with Low Carbohydrate High Protein diet. However, independently of the size of LDs, the tendency in decreasing the ratio of UFA/SFA due to the development of the disease is preserved [45].

Another marker of livers' condition observed via Raman spectroscopy is vitamin A stored in Hepatic Stellate Cells (HSC). It is commonly known, that during the first stage of liver injury HSCs become activated, the number of LDs increases but the amount of retinyl esters decreases, suggesting a crucial role of vitamin A in injury

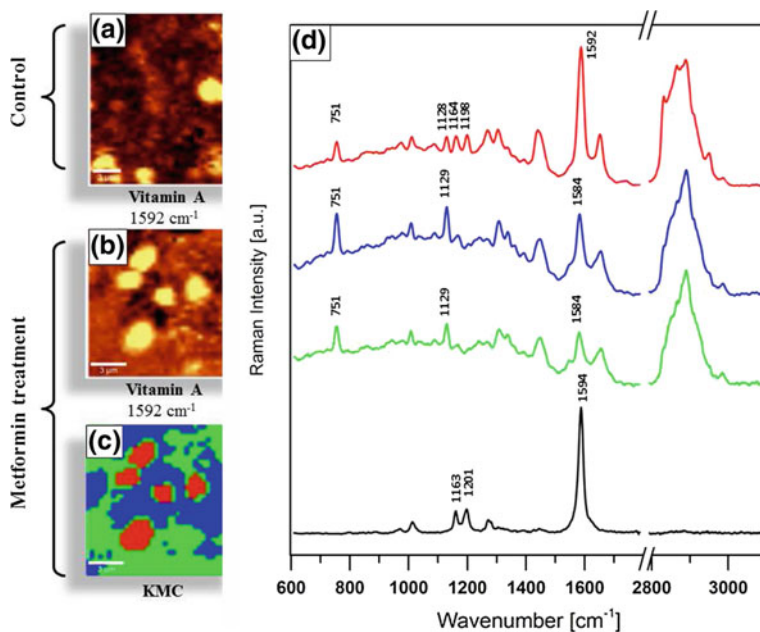


Fig. 14.21 Distribution of vitamin A: Analysis based on a marker band at $1594 \text{ rel. cm}^{-1}$ in: **a** control liver and **b** liver from mice with NAFLD, subjected to treatment with metformin. Results of K-means cluster analysis presented in **(c)**: KMC clusters along with **(d)** average spectra of clusters (red, blue, green) and spectrum of the standard of all-trans-retinol (black)

and liver repair process [57]. Vitamin A has been observed in samples of healthy liver tissue numerous times [45, 47, 58]. Detailed investigations of vitamin A content in healthy tissues was performed on liver sections obtained from C57BL/6J mice fed with a standard diet (AIN-93G). The presence of vitamin A can be clearly revealed by the marker band located at $1594 \text{ rel. cm}^{-1}$ (Fig. 14.21). The position of this band is close to one of three marker bands of heme ($\sim 751, 1130, 1585 \text{ rel. cm}^{-1}$), often observed in liver tissue spectra. However, the intensity of vitamin A signals greatly exceeds the intensity of any other components of liver tissue.

In addition, the spectrum of vitamin A exhibits two additional marker bands of lower intensity, at 1163 and $1201 \text{ rel. cm}^{-1}$ (Fig. 14.21). The majority of vitamin A in HSCs of healthy liver is in the form of all-trans-retinol [45]. In accordance with the above stated facts, vitamin A was not found in any of liver injury models. However, its presence was observed in liver samples from mice with the HFD-induced NAFLD, subjected to treatment with metformin. As discussed previously, metformin (a reference drug) therapy was proven to be effective. Small lipid accumulations, with characteristic signals from vitamin A were observed in metformin treated samples. The signals from vitamin A were of lower intensity than in control samples, suggesting a lower content of vitamin A. However, their reappearance in metformin treated samples indicate the rebuilding of vitamin A storage occurring as a result of the effective therapy.

14.3 Part II

14.3.1 *Experimental*

14.3.1.1 Cell Culture Protocols

EA.hy 926 cells, immortalized hybrids, were derived by fusion of Human Umbilical Vein Endothelial Cells (HUVEC) with human lung carcinoma cells line A549 [18]. EA.hy 926 cells were cultured in Dulbecco's modified Eagle's medium (DMEM, Lonza) supplemented with 10% fetal bovine serum (FBS), 1% penicillin-streptomycin, 2mM L-glutamine (Invitrogen) and 2% HAT medium supplement. Primary human aortic endothelial cells (HAoEC) were purchased from Gibco and cultured in supplemented endothelial cell growth medium (EGM-2 MV from Lonza). The cells were grown in 75 cm³ culture flasks (BD Falcon) and were incubated in a 37 °C, 5% CO₂/95% air, humidified cell culture incubator. For Raman measurements cells were directly grown on calcium fluoride slides (CaF₂, 25 × 2mm, Pike Technologies, U.S.) and after 24 h were fixed for 4 min with 4% paraformaldehyde or 2.5% glutaraldehyde and stored in isotonic phosphate buffer, pH = 7 at 4 °C until data acquisition. For Raman measurements the CaF₂ slides with cells were submerged in PBS.

14.3.1.2 Preparation of Blood Smears and Functional Erythrocytes

Capillary blood samples were obtained from healthy volunteers. 20 μL of fresh blood was transferred to an 80 mm diameter glass Petri dish filled with 10 mL of cold saline solution (around 5 °C). The Petri dish was pre-coated with gold and poly-L-lysine as previously described [59]. The cells were settled for around 10 min until a thin monolayer of blood cells was observed. Thin smears of whole blood were prepared by pinprick. The blood was smeared on the ethanol cleaned and dried CaF₂ windows to obtain a monolayer of blood cells. Such prepared blood smears were air-dried and selected areas were measured using Raman, AFM and scanning near-field optical microscopy (SNOM) (RBCs, leucocytes and blood plasma) [60].

14.3.1.3 Data Acquisition

Confocal Raman imaging was done using an alpha 300 Confocal Raman Imaging system (WITec GmbH, Ulm, Germany) as described in Sect. 14.2.1.2, with the application of a 60× water immersion objective (Nikon Fluor, NA = 1) or for dried blood smears a 100× air objective (Olympus, MPlan FL, NA = 0.9). Data acquisition was controlled by the WitecControl data acquisition software package.

14.3.1.4 Endothelial Cells

Raman spectra from endothelial cells were recorded using 488nm solid state laser (laser power of ca.15mW at the sample). Raman imaging of cells was performed by collecting spectra with 0.5 s exposure time and moving the sample in increments of 0.6 μ m (65 \times 40 μ m², 108 \times 66 points). The depth of cell profiling was 9 μ m (volume of 13 \times 28 \times 9 μ m³) measured as nine layers in a stack every 1.0 μ m in the z-direction from top to bottom. Each voxel of obtained 3D image represents a full Raman spectrum which was collected using 0.4 s exposure time and sampling density of 0.6 μ m (13 \times 28 \times 9 μ m³, 21 \times 46 \times 9 points). The total exposure time was ca.2 h [1 h per Raman image of the entire cell and additional 1 h for depth profiling of the selected area (7 min per layer)]. Cells were submerged in PBS during the measurement.

14.3.1.5 Red Blood Cells

Results for functional RBCs as well as air-dried smears were obtained using 488 and 532nm laser excitations. The integration time for a single spectrum was 0.3s and the spectral resolution was equal to 1 or 3 rel. cm⁻¹ (depending on the grating used, 1800grooves/mm or 600grooves/mm, respectively). The laser power used varied from 9 μ W to 5mW. The AFM measurements were performed in the AC mode using standard force modulation probes (WITec, Ulm, Germany) with a nominal spring constant of 2.8N/m and the resolution 256 \times 256 points per 20 \times 20 μ m. The SNOM measurements were carried out using cantilever SNOM sensors (WITec) with a <100nm aperture diameter, an excitation laser wavelength of 488nm and with a resolution of 256 \times 256 points per 10 \times 10 μ m.

14.3.1.6 Data Processing

Raman, AFM and SNOM data analysis were performed using WITecProject Plus software package (Version 2.10). All spectra were baseline corrected using a 2nd order polynomial (for liver cells) or 3rd order polynomial (for endothelial cells) and the routine procedure for cosmic rays removal was applied. Raman distribution images of selected compounds or groups of compounds were obtained based on integration of corresponding marker bands. Cluster analysis was performed using the K-means method with Manhattan distance. The Image J processing program was used to obtain 3D pictures of cells [22]. For calculations of the area occupied by cells and cell nuclei, the Matlab software was used.

14.3.2 Results and Discussions

14.3.2.1 3D Raman Imaging of Single Endothelial Cells

3D-approach for cell analysis is a novel trend in analytical spectroscopy, which allows determination of the biochemical composition at the subcellular level with a high spatial (both lateral and depth) resolution [61].

Taking into account the small size of endothelial cells and their heterogeneous biochemical composition, significant spectral changes along few microns of depth profiling were expected within a cell (Fig. 14.22). Two-dimensional spectral images calculated by integrating the intensity of the C–H stretching vibrations in the 2800–3020 rel. cm^{-1} range were acquired (Fig. 14.22b). Bright and dark regions are related mainly to differences in protein and lipid density, water content and sample thickness. For Fig. 14.22d, e the same colour scaling was provided to allow the reader to judge the overall relative concentration of selected compounds. Raman spectra obtained from the same point of each imaged layer of the cell is presented in Fig. 14.22f (500–1800 rel. cm^{-1} range). Spectra were selected from the nucleoli area in the xy-plane. Based on extracted spectra (Fig. 14.22f) and Raman images obtained by integration of the 1630–1690 rel. cm^{-1} spectral range (Fig. 14.22e), the variation in the intensity of the registered spectra was observed between layers.

Most information about the chemical composition of biological samples can be found in the fingerprint range (400–1800 rel. cm^{-1}). The presence of proteins manifests itself in the Raman spectra by two characteristic bands, Amide I and Amide III, which are sensitive to the secondary structure of proteins. Generally, information on the content and structure of proteins in the cells can be obtained by the analysis of position and intensity of the following bands: approx. 1660 rel. cm^{-1} (Amid I), 1450 rel. cm^{-1} (CH_2 bending), 1100–1375 rel. cm^{-1} (Amid III) and ~ 1005 rel. cm^{-1} (phenylalanine). The lipid composition of cells can be determined based on the bands: 1740 rel. cm^{-1} (C=O); 1656 rel. cm^{-1} (cis C=C); 1441 rel. cm^{-1} (CH_2 bending) and 1304 rel. cm^{-1} (CH_2 twisting). An informative spectral observation is also the density of the investigated area of the sample, e.g. cytoplasm can be recognised in the spectra by the noticeably lower signal to noise ratio (especially in the fingerprint range).

The high wavenumber range (2800–3030 rel. cm^{-1}) provides information on the protein-lipid composition. The intensity of bands at 3005–3015 rel. cm^{-1} (stretching vibrations of the =C–H bonds) can be correlated with the amount of double bonds in the molecules of lipids/fatty acids. The spectral difference associated with lipids can be tracked by analyzing the bands in the range of 2850–2900 rel. cm^{-1} , that is more useful for the areas of the cytoplasm around the nucleus (endoplasmic reticulum and mitochondria).

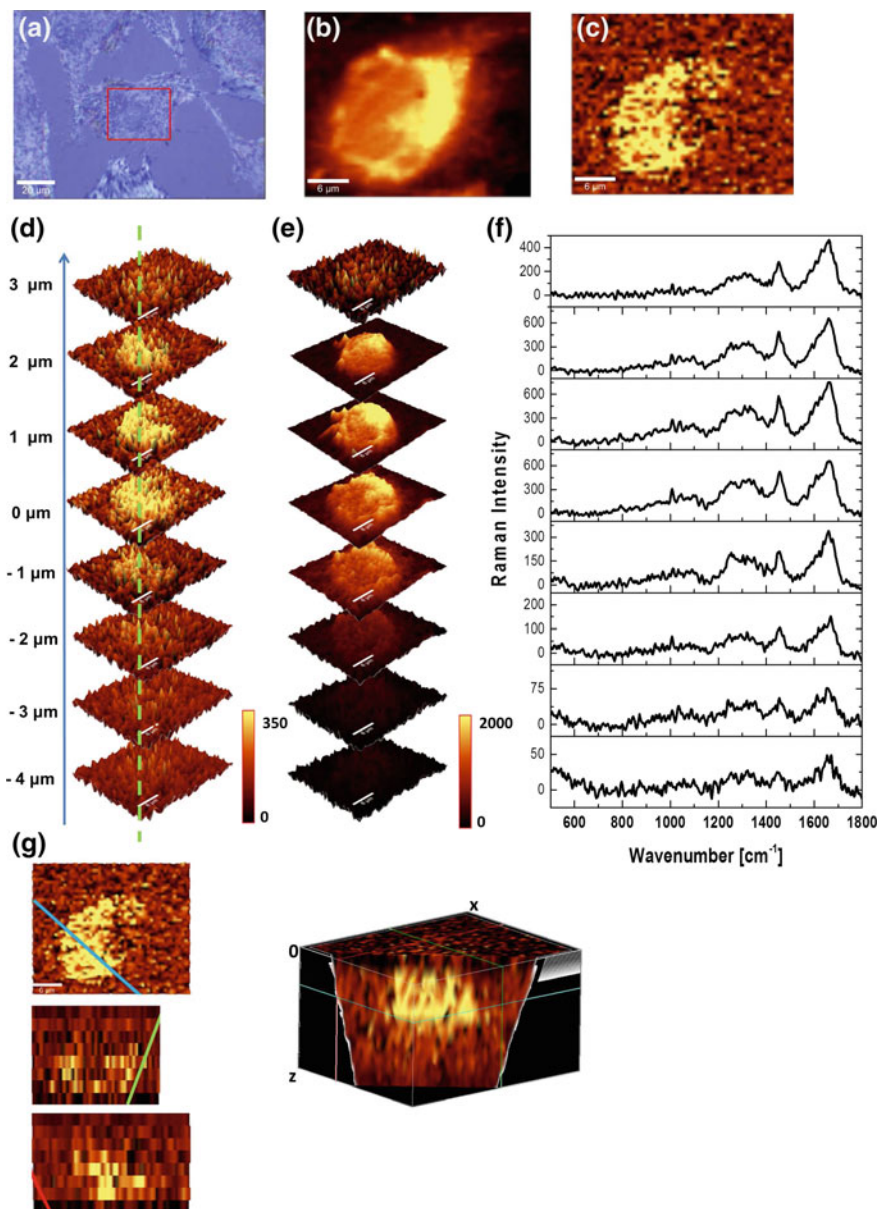


Fig. 14.22 Confocal Raman imaging-stack of an endothelial cell ($33 \times 27 \mu\text{m}$, 55×45 points). The visual image ($\times 60$, **a**), integration images of the third layer (**b**, **c**) obtained by integration of the ν_{C-H} and ring breathing modes in the DNA/RNA bases bands ($2800\text{--}3020$ and $760\text{--}805$ rel. cm^{-1} range, respectively), an imaging-stack of the endothelial cell covering $33 \times 27 \times 8 \mu\text{m}^3$ of the cell (integration images in the $760\text{--}805$ (**d**) and $1630\text{--}1690$ rel. cm^{-1} (**e**) range), single spectra (**f**) extracted from the same point of the images (green dotted line in **d**), a reconstructed 3D image - a cross-section of the reconstructed 3D image (volumes within a 3D-(xyz)-space) with intersection in xy-, zy- and xz-planes (**g**). Scale bars: $20 \mu\text{m}$ for (**a**), $6 \mu\text{m}$ for (**b**–**f**)

The reconstructed three dimensional cell image is presented in Fig. 14.22g as a volume within a xyz-coordination system. By using the volume viewer option and rendering with intersection in xy-, zy- and xz-plane it was possible to obtain cross-sections of the cell together with selected subcellular structures [61]. These results show that by using confocal Raman imaging it was possible to define the size, volume, shape and biochemical composition of selected cellular components inside a single cell without the need for special sample preparation.

14.3.2.2 Confocal Raman Imaging of Lipid Droplets Formed in Endothelium

We have shown that endothelial cells are able to take up exogenous polyunsaturated fatty acids (PUFAs) and to form lipid droplets (LDs) [55, 62]. Moreover, 1-methylnicotinamide (MNA) facilitates this process and increases the number of endothelial LDs [62].

LDs can be identified using Raman spectroscopy by characteristic bands (Fig. 14.23f), at $1660 \text{ rel. cm}^{-1}$ and $\sim 3015 \text{ rel. cm}^{-1}$ due to the stretching mode of the C=C bonds and =C-H bonds associated with the C=C double bonds [55]. In Fig. 14.23 two-dimensional spectral images calculated by integrating the intensity of the C-H stretching vibrations of aliphatic molecules in the $2800\text{--}3020 \text{ rel. cm}^{-1}$ range (Fig. 14.23b), cytosine ring breathing vibrations of DNA in $775\text{--}790 \text{ rel. cm}^{-1}$ range (Fig. 14.23c) and =CH-stretching vibrations in $3000\text{--}3030 \text{ rel. cm}^{-1}$ range (Fig. 14.23d) are shown. Additionally, confocal Raman imaging was used as

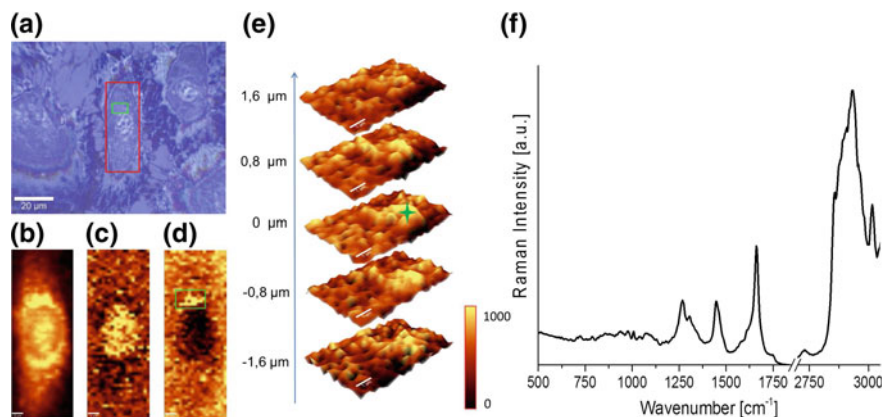


Fig. 14.23 Confocal Raman imaging of the HAoEC cell with LDs. The full area of the cell [(a), red square] with the zoomed area (marked in green), images obtained by integration of the $3000\text{--}3030 \text{ rel. cm}^{-1}$ (b), $760\text{--}805 \text{ rel. cm}^{-1}$ (c) and $3000\text{--}3030 \text{ rel. cm}^{-1}$ (d) ranges, imaging-stack of LDs (e) covering $8 \times 5 \times 4.2 \mu\text{m}^3$ of cell (green square in (a)); images obtained by integration of the $1630\text{--}1690 \text{ rel. cm}^{-1}$ range), single Raman spectrum of a LD (f). Scale bars: $20 \mu\text{m}$ for (a), $3 \mu\text{m}$ for (b–d) and $1 \mu\text{m}$ for (f). The same colour scaling (min - 0, max - 450) was provided to help to judge the overall concentration of lipids

a non-invasive tool to illustrate the 3D distribution of LDs in the single endothelial cell (Fig. 14.23e). Comparison of the LDs' average spectrum (Fig. 14.23f) with standards of selected unsaturated fatty acids [63] allows an approximation of biochemical composition of these lipidic structures. The bands at 1447, 1658, 1736, 2855 and 3015 rel. cm^{-1} have been assigned to PUFAs and detailed analysis of LDs average spectrum suggests that the main component of LDs is arachidonic acid [62].

Lipid droplets formation upon the unsaturated fatty acid uptake was studied in the context of their structure and content. In the literature investigation of LDs formation in various cells using Raman spectroscopy, including also more involved techniques such as coherent anti-stokes Raman scattering (CARS) microscopy, has been reported [64–68]. It has also been demonstrated that stimulation of endothelial cells using arachidonic acid (a precursor of prostacyclin (PGI_2) and other prostaglandins) and 1-methylnicotinamide leads to formation of LDs in high amount [62]. A similar cell response was observed for eicosapentanoic acid (EPA). Altogether it has been shown that Raman spectroscopy is applicable to study LDs in situ, that helped to demonstrate a novel biological context of LD formation in the endothelium, of potential physiological significance.

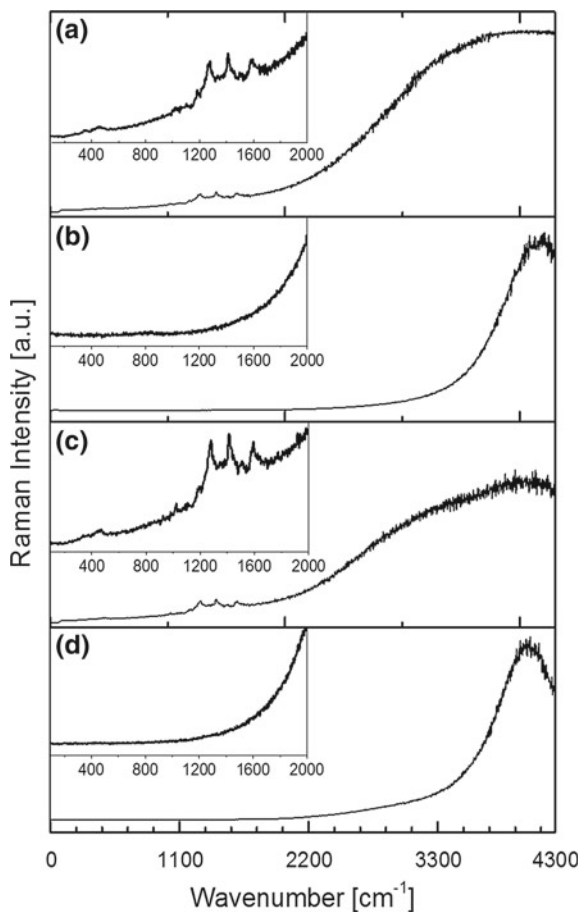
14.3.2.3 Single Endothelial Cells Exposed on Anthracycline

Raman imaging represents a new methodological approach in pharmacology, since it provides information on the biochemical changes occurring in endothelial cells at the subcellular level following their exposure to anthracyclines antibiotics. Raman spectra of investigated anthracyclines (doxorubicin (DOX), daunorubicin (DNR), epidoxorubicin (EDOX), epidaunorubicin (EDNR)) are shown in Fig. 14.24.

By using the excitation in the 400–550nm range, the resonance Raman spectra of anthracyclines can be recorded [69, 70]. However, these compounds exhibit strong fluorescence, which can be observed in Raman spectra as an increased background in the high wavenumber range (maximum at approx. 3800–4200 rel. cm^{-1}).

To study an impact of anthracyclines on endothelium, the cells (EA.hy 926 line) were incubated for 24 h with DOX, DNR, EDOX and EDNR, at the concentrations in the range of 100nM–1 μm . It is known that the cytostatic function of anthracyclines is related to the formation of a stable complex with the DNA helix, which prevents further division and leads to cell death, so the analysis of changes in the cell nucleus was carried out. Since the spectral range of the maximum anthracycline fluorescence coincides with the raised background of anthracycline-stimulated cells (3800–4200 rel. cm^{-1}), it seems to be the best spectral marker of the presence of anthracyclines in the cell. Therefore, the integration of this spectral range allowed for studying the distribution of anthracyclines in the cells. Figure 14.25 shows the results of integration of the marker range (3820–4200 rel. cm^{-1}) for cells stimulated with anthracyclines at the concentrations of 100nM–1 μm .

Fig. 14.24 Raman spectra of studied anthracyclines: **a** daunorubicin (DNR), **b** doxorubicin (DOX), **c** epidaunorubicin (EDNR) and **d** epidoksorubicin (EDOX) in full spectral range and magnification of the 100–2000 cm^{-1} range. Spectra of anthracyclines (powder) recorded using the 488nm laser line



Integration of the marker spectral range of anthracyclines showed that DNR and EDOX accumulates in the nucleus beginning from a concentration of 300nM. The presence of EDNR in a cell can be observed at higher doses, i.e. 500nM, therefore the epimer of toxic DNR seems to be an interesting candidate as a chemotherapeutic agent from the point of view of low accumulation in endothelium. Additionally, accumulation of anthracyclines overlapped the nucleus area (DNA distribution) [71, 72].

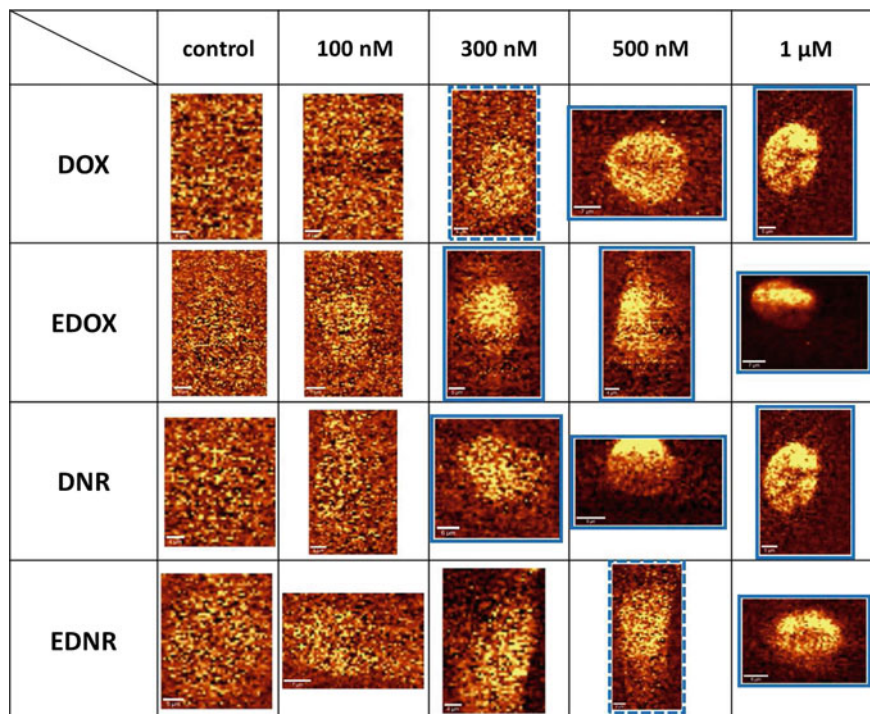


Fig. 14.25 Representative images obtained by integration of the 3820–4245 rel. cm^{-1} range (spectral range of anthracycline maximum fluorescence). “Threshold concentrations” (the lowest concentration for which the accumulation of anthracyclines in the nucleus was observed) are marked with a blue square (dashed line indicates these concentrations of the drugs for which part of the cells exhibit slight and ambiguous background increasing due to antibiotic fluorescence)

14.3.2.4 Raman Spectroscopy and Complementary Techniques in Red Blood Cells Analysis

Raman spectroscopy was successfully used for studies of standard hematoporphyrin as well as for imaging of heme, both in cells and tissues [73]. Functional as well as air-dried RBCs can be investigated by that method. The resonance Raman spectrum of hemoglobin (Hb) is observed when this compound is irradiated with the laser line, which corresponds to the wavelength of an electronic transition of Hb (488 and 532nm). Moreover, it has been previously suggested that the highly aligned structural arrangement of Hb inside functional RBCs causes a significant increase in the non-fundamental modes of the Raman spectra when excitation line is in close proximity to the vibronic band Q_v (observed for 514.5 and 532nm excitation laser lines). It was reported that bands associated with oxyHb in malaria-infected RBCs can be identified more readily in the non-fundamental region [74].

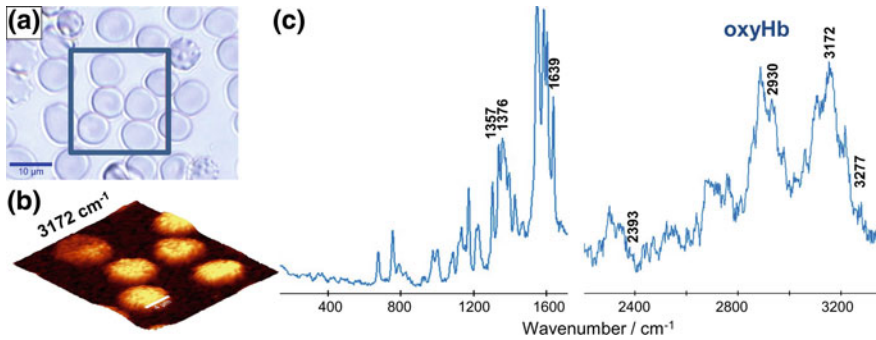


Fig. 14.26 Raman imaging of oxyHb in functional RBCs with the use of the overtone region band: **a** A photomicrograph of the live RBCs with the investigated area outlined (blue); **b** A Raman image obtained by integration of the oxyHb band in the overtone region at $3172 \text{ rel. cm}^{-1}$ (ν_4); **c** the average resonant Raman spectra of oxyHb inside RBC obtained with the excitation of 532 nm . Figure adapted with permission from [74]. Copyright (2014) John Wiley & Sons, Inc.

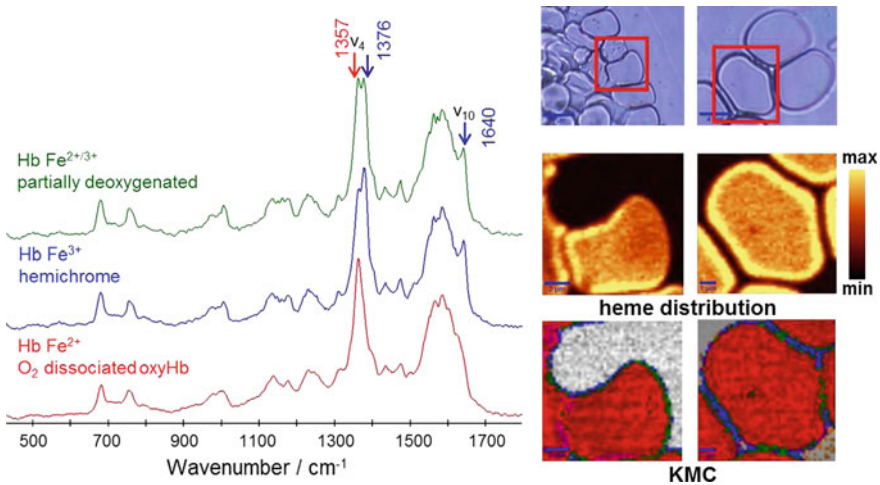


Fig. 14.27 High-resolution Raman imaging reveals spatial location of heme oxidation sites in single red blood cells of dried smears. A photomicrographs of the selected area of the air-dried human RBCs (whole blood, smear on the CaF_2 slide) with the labelled (red) investigated area; Raman images obtained by integration of the Hb's band in the spectral region of around $1350\text{--}1380 \text{ rel. cm}^{-1}$ (ν_4); KMC results with three main clusters for RBCs. The clusters include hemichrome Hb Fe^{3+} (blue), laser-induced O_2 dissociated oxyHb, Hb Fe^{2+} (red) and partially deoxygenated Hb $\text{Fe}^{2+/3+}$ (green). The grey cluster observed between RBC's corresponds to substrate signal and is removed as an outlier. The representative spectra of the obtained clusters of RBCs obtained from the K-means Clustering (KMC). Figure adapted with permission from [60]. Copyright (2014) John Wiley & Sons, Inc.

The use of both, fundamental and overtone Raman regions improved the diagnostic capability of the Raman technique for malaria disease [74]. Figure 14.26 presents the Raman image obtained by integration of the overtone at $3172 \text{ rel. cm}^{-1}$ of oxyHb of functional RBCs.

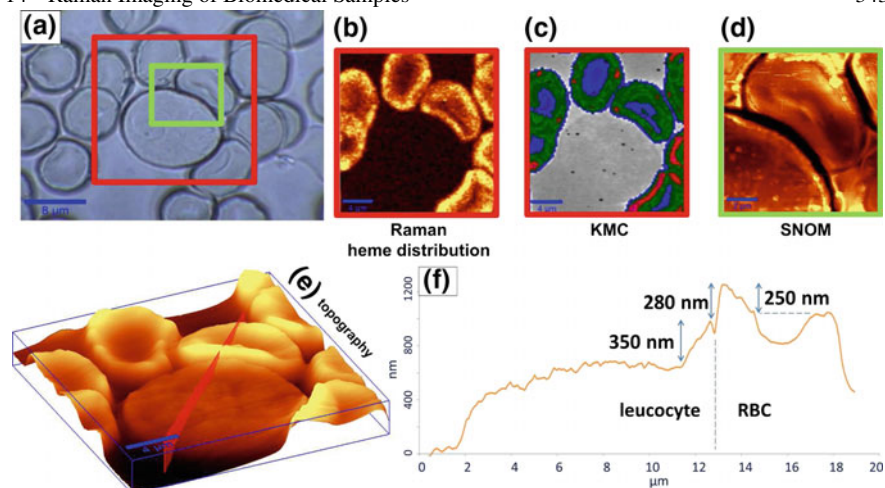


Fig. 14.28 Raman, AFM and SNOM as complementary techniques: **a** A photomicrograph of the air-dried human RBCs around a single leucocyte with the investigated area by Raman and AFM (red) as well as SNOM (green); **b** A Raman image obtained by integration of the Hb band in the spectral region around $1350\text{--}1380\text{rel. cm}^{-1}$ (ν_4); **c** A KMC image of Fe^{2+} and Fe^{3+} distribution - colour coding as in Fig. 14.27; **d** SNOM results; **e** AFM topography image; **f** Topography cross section according to the red line presented in (e). Figure adapted with permission from [60]. Copyright (2014) John Wiley & Sons, Inc.

In analogy to functional RBCs, also for dried RBCs, which are measured in ambient conditions, the majority of the hemoglobin (Hb) exists in the oxyHb state. However, the studies of the thin smears of whole blood with the use of high-resolution Raman imaging shows also the hemichrome in the thin outer layer of RBCs [60]. To image the presence of the different heme type inside RBCs, 488nm excitation and laser-induced photo/thermal-dissociation of O_2 from oxyHb was used. The laser induced dissociation of oxyHb (Fe^{3+} , low spin) produces deoxyHb (Fe^{2+} , high spin). The observed hemichrome is a bishistidine complex, which does not contain the O_2 molecule, so no change to Fe^{2+} is observed in the regions where hemichrome is present [60].

The resonance Raman spectra allowed for observation of the oxidation state marker band (ν_4 mode), which changes from 1376 to 1357rel. cm^{-1} for Fe^{3+} and Fe^{2+} Hb, respectively [75]. Figure 14.27 presents the visualization of the hemichrome inside air-dried RBCs with the representative Raman spectra.

The visualization of distribution of $\text{Fe}^{2+/3+}$ heme was studied also for RBCs in direct contact with some leucocytes (Fig. 14.28). This studies were supported with the AFM and SNOM techniques. AFM enabled the measurement of the RBCs-leucocyte topography that was very useful for the determination of the necessary size of the Raman imaging stack. SNOM results provided the information about the existence of the fluorophore compound in the area of the contact between RBC and leucocyte.

14.4 Summary and Outlook

Modern confocal Raman microscopy becomes an increasingly important tool in biological and medical sciences, due to the lateral resolution close to the Rayleigh limit and a high throughput. Raman imaging of cells and tissues yields a plethora of information about the distribution of biocomponents, their molecular structures and interactions between them. Therefore, Raman imaging is a suitable tool to study mechanisms of pathology development in model systems, such as cell cultures *in vitro* or tissues *ex vivo*.

This chapter summarizes our recent research focusing on application of Raman imaging to study murine models of lifestyle diseases, i.e. type 2 diabetes mellitus, hypertension, metastatic cancer, atherosclerosis, and non-alcoholic fatty liver disease. Moreover, the suitability of Raman microscopy for the characterization of biocomponents as well as processes of biomolecules and drugs uptake in single cells is also demonstrated. Several examples of successful combinations of Raman imaging with other complementary methods such as AFM or SNOM as well as applications of 3D imaging are also presented.

Raman microscopy is a unique probe to study cellular processes and chemical alterations in tissues due to pathology. It is expected that this technique, at the moment used mostly as a research tool in model systems, in the future may become a routine method of medical diagnostics, for example in cytopathology or a non-invasive investigation of disease margins.

Acknowledgements The financial support by National Science Centre (DEC-2013/08/A/ST4/00308) and by the European Union under the European Regional Development Fund (grant coordinated by JCET-UJ, POIG.01.01.02-00-069/09) is acknowledged.

References

1. J. Peloquin, J. Huynh, R.M. Williams, C.A. Reinhart-King, *J. biomechanics* **44**(5), 815 (2011)
2. J. Clark, S. Glagov, *Br. J. Exp. Pathol.* **57**(1), 129 (1976)
3. U. Smith, J.W. Ryan, D.D. Michie, D.S. Smith, *Science* **173**(4000), 925 (1971)
4. K. Kusche-Vihrog, K. Urbanova, A. Blanqué, M. Wilhelmi, H. Schillers, K. Kliche, H. Pavenstädt, E. Brand, H. Oberleithner, *Hypertension* **57**(2), 231 (2011)
5. H. Oberleithner, W. Peters, K. Kusche-Vihrog, S. Korte, H. Schillers, K. Kliche, K. Oberleithner, *Pflügers Arch.-Eur. J. Physiol.* **462**(4), 519 (2011)
6. M. Pilarczyk, A. Rygula, A. Kaczor, L. Mateuszuk, E. Maślak, S. Chlopicki, M. Baranska, *Vib. Spectrosc.* **75**, 39 (2014)
7. M.Z. Pacia, E. Buczek, A. Blazejczyk, A. Gregorius, J. Wietrzyk, S. Chlopicki, M. Baranska, A. Kaczor, *Anal. Bioanalytical Chem.* **408**(13), 3381 (2016)
8. M. Pilarczyk, A. Rygula, L. Mateuszuk, S. Chlopicki, M. Baranska, A. Kaczor, *Biomed. Spectrosc. Imaging* **2**(3), 191 (2013)
9. K.W. Short, S. Carpenter, J.P. Freyer, J.R. Mourant, *Biophys. J.* **88**(6), 4274 (2005)
10. C. Krafft, T. Knetschke, R.H. Funk, R. Salzer, *Anal. Chem.* **78**(13), 4424 (2006)
11. B.R. Wood, B. Tait, D. McNaughton, *Biochimica et Biophysica Acta (BBA)-Molecular. Cell Res.* **1539**(1), 58 (2001)
12. K. Meister, J. Niesel, U. Schatzschneider, N. Metzler-Nolte, D.A. Schmidt, M. Havenith, *Angew. Chem. Int. Ed.* **49**(19), 3310 (2010)

13. H.J. van Manen, C. Otto, *Nano lett.* **7**(6), 1631 (2007)
14. M. Davoren, E. Herzog, A. Casey, B. Cottineau, G. Chambers, H.J. Byrne, F.M. Lyng, *Toxicol. In Vitro* **21**(3), 438 (2007)
15. P. Candeloro, L. Tirinato, N. Malara, A. Fregola, E. Casals, V. Puntès, G. Perozziello, F. Gentile, M.L. Coluccio, G. Das et al., *Analyst* **136**(21), 4402 (2011)
16. C. Scalfi-Happ, M. Udart, C. Hauser, A. Rück, *Med. Laser Appl.* **26**(4), 152 (2011)
17. T. Chernenko, C. Matthäus, L. Milane, L. Quintero, M. Amiji, M. Diem, *ACS Nano* **3**(11), 3552 (2009)
18. C. Matthäus, T. Chernenko, J.A. Newmark, C.M. Warner, M. Diem, *Biophys. J.* **93**(2), 668 (2007)
19. H. Yao, Z. Tao, M. Ai, L. Peng, G. Wang, B. He, Y.Q. Li, *Vib. Spectrosc.* **50**(2), 193 (2009)
20. Z. Liu, K. Chen, C. Davis, S. Sherlock, Q. Cao, X. Chen, H. Dai, *Cancer Res.* **68**(16), 6652 (2008)
21. D.M. Stitt, M.Z. Kastyak-Ibrahim, C.R. Liao, J. Morrison, B.C. Albensi, K.M. Gough, *Vib. Spectrosc.* **60**, 16 (2012)
22. W. Rasband, <http://rsb.info.nih.gov/ij> pp. 1997–2007 (1997)
23. H. Chen, O. Charlat, L.A. Tartaglia, E.A. Woolf, X. Weng, S.J. Ellis, N.D. Lakey, J. Culpepper, K.J. More, R.E. Breitbart et al., *Cell* **84**(3), 491 (1996)
24. M. Pilarczyk, L. Mateuszuk, A. Rygula, M. Kepczynski, S. Chlopicki, M. Baranska, A. Kaczor, *PLoS ONE*; e106065. **9**(8) (2014). <https://doi.org/10.1371/journal.pone.0106065>
25. C. Krafft, L. Neudert, T. Simat, R. Salzer, *Spectrochim. Acta Part A: Mol. Biomol. Spectrosc.* **61**(7), 1529 (2005)
26. K. Simons, D. Toomre, *Nat. Rev. Mol. Cell Biol.* **2**(3), 216 (2001)
27. K. Simons, M.J. Gerl, *Nat. Rev. Mol. Cell Biol.* **11**(10), 688 (2010)
28. H. Cai, D.G. Harrison, *Circ. Res.* **87**(10), 840 (2000)
29. H.D. Intengan, E.L. Schiffrin, *Hypertension* **38**(3), 581 (2001)
30. M.Z. Pacia, L. Mateuszuk, S. Chlopicki, M. Baranska, A. Kaczor, *Analyst* **140**(7), 2178 (2015)
31. M. Gniadecka, P.A. Philipsen, S. Sigurdsson, S. Wessel, O.F. Nielsen, D.H. Christensen, J. Hercogova, K. Rossen, H.K. Thomsen, R. Gniadecki et al., *J. Invest. Dermatol.* **122**(2), 443 (2004)
32. K. Majzner, T.P. Wrobel, A. Fedorowicz, S. Chlopicki, M. Baranska, *Analyst* **138**(24), 7400 (2013)
33. J. Suh, M. Moskovits, *J. Am. Chem. Soc.* **108**(16), 4711 (1986)
34. B.G. Frushour, J.L. Koenig, *Biopolymers* **14**(2), 379 (1975)
35. M.M. Steed, N. Tyagi, U. Sen, D.A. Schuschke, I.G. Joshua, S.C. Tyagi, *Am. J. Physiol.-Lung Cell. Mol. Physiol.* **299**(3), L301 (2010)
36. S. Duraipandian, W. Zheng, J. Ng, J.J. Low, A. Ilancheran, Z. Huang, *Analyst* **136**(20), 4328 (2011)
37. E.M. Kanter, S. Majumder, E. Vargis, A. Robichaux-Viehoever, G.J. Kanter, H. Shappell, H.W. Jones III, A. Mahadevan-Jansen, *J. Raman Spectrosc.* **40**(2), 205 (2009)
38. A. Robichaux-Viehoever, E. Kanter, H. Shappell, D. Billheimer, H. Jones III, A. Mahadevan-Jansen, *Appl. Spectrosc.* **61**(9), 986 (2007)
39. J.W. Franses, N.C. Drosu, W.J. Gibson, V.C. Chitalia, E.R. Edelman, *Int. J. Cancer* **133**(6), 1334 (2013)
40. S. Dalaklioglu, A. Tasatargil, S. Kale, G. Tanriover, S. Dilmac, N. Erin, *Vasc. Pharmacol.* **59**(3), 103 (2013)
41. E. Buczek, A. Blazejczyk, T. Wojcik, B. Sitek, L. Mateuszuk, A. Jaształ, E. Maslak, A. Fedorowicz, B. Proniewski, R. Gurbiel, J. Wietrzyk, S. Chlopicki, *BMC Cancer* **in review** (2016)
42. T. Wrobel, A. Fedorowicz, L. Mateuszuk, E. Maslak, A. Jaształ, S. Chlopicki, K. Marzec, *Vibrational Microspectroscopy for Analysis of Atherosclerotic Arteries* (Springer, Dordrecht, 2014), pp. 505–535
43. K.M. Marzec, A. Rygula, M. Gasiór-Głogowska, K. Kochan, K. Czamara, K. Bulat, K. Malek, A. Kaczor, M. Baranska, *Pharmacol. Rep.* (2015)

44. K.M. Marzec, T.P. Wrobel, A. Rygula, E. Maslak, A. Jaształ, A. Fedorowicz, S. Chłopicki, M. Baranska, *J. Biophotonics* **7**(9), 744 (2014)
45. K. Kochan, K. Marzec, E. Maslak, S. Chłopicki, M. Baranska, *Analyst* **140**(7), 2074 (2015)
46. T. Wrobel, K. Marzec, S. Chłopicki, E. Maślak, A. Jaształ, M. Franczyk-Żarów, I. Czyżyńska-Cichoń, T. Moszkowski, R. Kostogryś, M. Baranska, *Sci. Rep.* **5** (2015)
47. K. Kochan, K.M. Marzec, K. Chruszcz-Lipska, A. Jaształ, E. Maslak, H. Musiolik, S. Chłopicki, M. Baranska, *Analyst* **138**(14), 3885 (2013)
48. K. Marzec, K. Kochan, A. Fedorowicz, A. Jaształ, K. Chruszcz-Lipska, J.C. Dobrowolski, S. Chłopicki, M. Baranska, *Analyst* **140**(7), 2171 (2015)
49. A. Rygula, M. Pacia, L. Mateuszuk, A. Kaczor, R. Kostogryś, S. Chłopicki, M. Baranska, *Analyst* **140**(7), 2185 (2015)
50. Y. Takahashi, Y. Soejima, T. Fukusato, *World J. Neurogastroenterol: WJG* **18**(19), 2300 (2012)
51. A.M. Zivkovic, J.B. German, A.J. Sanyal, *Am. J. Clin. Nutr.* **86**(2), 285 (2007)
52. G. Kanuri, I. Bergheim, *Int. J. Mol. Sci.* **14**(6), 11963 (2013)
53. R. Buettner, K. Parhofer, M. Woenckhaus, C. Wrede, L. Kunz-Schughart, J. Schölmerich, L. Bollheimer, *J. Mol. Endocrinol.* **36**(3), 485 (2006)
54. O. Samek, A. Jonáš, Z. Pilát, P. Zemánek, L. Nedbal, J. Tříška, P. Kotas, M. Trtílek, *Sensors* **10**(9), 8635 (2010)
55. K. Majzner, K. Kochan, N. Kachamakova-Trojanowska, E. Maslak, S. Chłopicki, M. Baranska, *Anal. Chem.* **86**(13), 6666 (2014)
56. E. Maslak, P. Zabielski, K. Kochan, K. Kus, A. Jaształ, B. Sitek, B. Proniewski, T. Wojcik, K. Gula, A. Kij et al., *Biochem. Pharmacol.* **93**(3), 389 (2015)
57. N. Testerink, M. Ajat, M. Houweling, J.F. Brouwers, V.V. Pully, H.J. van Manen, C. Otto, J.B. Helms, A.B. Vaandrager, *PLoS ONE* **7**(4), e34945 (2012)
58. K. Galler, F. Schleser, E. Fröhlich, R.P. Requardt, A. Kortgen, M. Bauer, J. Popp, U. Neugebauer, *Integr. Biol.* **6**(10), 946 (2014)
59. B.R. Wood, L. Hammer, L. Davis, D. McNaughton, *J. Biomed. Opt.* **10**(1), 014005 (2005)
60. K.M. Marzec, A. Rygula, B.R. Wood, S. Chłopicki, M. Baranska, *J. Raman Spectrosc.* **46**(1), 76 (2015)
61. K. Majzner, A. Kaczor, N. Kachamakova-Trojanowska, A. Fedorowicz, S. Chłopicki, M. Baranska, *Analyst* **138**(2), 603 (2013)
62. K. Majzner, S. Chłopicki, M. Baranska, *J. Biophotonics* **10**, 1 (2015)
63. K. Czamara, K. Majzner, M. Pacia, K. Kochan, A. Kaczor, M. Baranska, *J. Raman Spectrosc.* **46**(1), 4 (2015)
64. X. Nan, J.X. Cheng, X.S. Xie, *J. Lipid Res.* **44**(11), 2202 (2003)
65. C.W. Freudiger, W. Min, B.G. Saar, S. Lu, G.R. Holtom, C. He, J.C. Tsai, J.X. Kang, X.S. Xie, *Science* **322**(5909), 1857 (2008)
66. T.T. Le, S. Yue, J.X. Cheng, *J. Lipid Res.* **51**(11), 3091 (2010)
67. C. Nieva, M. Marro, N. Santana-Codina, S. Rao, D. Petrov, A. Sierra, *PLoS ONE*; e46456. <https://doi.org/10.1371/journal.pone.0046456>, **7**(10) (2012)
68. M.N. Slipchenko, T.T. Le, H. Chen, J.X. Cheng, *J. Phys. Chem. B* **113**(21), 7681 (2009)
69. Q. Yan, W. Priebe, J.B. Chaires, R.S. Czernuszewicz, *Biospectroscopy* **3**(4), 307 (1997)
70. G. Das, A. Nicastrì, M.L. Coluccio, F. Gentile, P. Candeloro, G. Cojoc, C. Liberale, F. De Angelis, E. Di Fabrizio, *Microsc. Res. Tech.* **73**(10), 991 (2010)
71. T. Wojcik, E. Buczek, K. Majzner, A. Kolodziejczyk, J. Miszczyk, P. Kaczara, W. Kwiatek, M. Baranska, M. Szymonski, S. Chłopicki, *Toxicol. In Vitro* **29**(3), 512 (2015)
72. K. Majzner, T. Wojcik, E. Szafraniec, M. Lukawska, I. Oszczapowicz, S. Chłopicki, M. Baranska, *Analyst* **140**(7), 2302 (2015)
73. D. McNaughton, B.R. Wood, T.C. Cox, J.C. Drenckhahn, in *Infrared and Raman Spectroscopic Imaging*, ed. by R. Salzer, H.W. Siesler (Wiley-VCH Verlag GmbH & Co. KGaA, 2009), pp. 203–220
74. K.M. Marzec, D. Perez-Guita, M. De Veij, D. McNaughton, M. Baranska, M.W. Dixon, L. Tilley, B.R. Wood, *Chem. Phys. Chem.* **15**(18), 3963 (2014)
75. A. Rygula, K. Majzner, K. Marzec, A. Kaczor, M. Pilarczyk, M. Baranska, *J. Raman Spectrosc.* **44**(8), 1061 (2013)